

2

NRL Memorandum Report 5453

AD-A148 504

# Propagation and Scattering Considerations for the 0.2-3.0 GHz Frequency Range for a Space-Based Radar

H. J. BILOW  
*Electromagnetics Branch  
Radar Division*

December 18, 1984

DTIC  
ELECTE  
DEC 17 1984  
B

DTIC FILE COPY



NAVAL RESEARCH LABORATORY  
Washington, D.C.

Approved for public release; distribution unlimited.

84 12 07 012

REPORT DOCUMENTATION PAGE				
1a REPORT SECURITY CLASSIFICATION <b>UNCLASSIFIED</b>		7d RESTRICTIVE MARKINGS		
2a SECURITY CLASSIFICATION AUTHORITY		3 DISTRIBUTION/AVAILABILITY OF REPORT		
2b DECLASSIFICATION/DOWNGRADING SCHEDULE		Approved for public release; distribution unlimited.		
4 PERFORMING ORGANIZATION REPORT NUMBER(S) <b>NRL Memorandum Report 5453</b>		5 MONITORING ORGANIZATION REPORT NUMBER(S)		
6a NAME OF PERFORMING ORGANIZATION <b>Naval Research Laboratory</b>	6b OFFICE SYMBOL (if applicable) <b>Code 5316</b>	7a NAME OF MONITORING ORGANIZATION		
6c ADDRESS (City, State, and ZIP Code) <b>Washington, DC 20375-5000</b>		7b ADDRESS (City, State, and ZIP Code)		
8a NAME OF FUNDING/SPONSORING ORGANIZATION <b>Naval Electronic Systems Command</b>	8b OFFICE SYMBOL (if applicable)	9 PROCUREMENT INSTRUMENT IDENTIFICATION NUMBER		
8c ADDRESS (City, State, and ZIP Code) <b>Washington, DC 20360</b>		10 SOURCE OF FUNDING NUMBERS		
		PROGRAM ELEMENT NO <b>62712N</b>	PROJECT NO	TASK NO <b>XF12-141-100</b>
				WORK UNIT ACCESSION NO <b>DN360-101</b>
11 TITLE (Include Security Classification) <b>Propagation and Scattering Considerations for the 0.2-3.0 GHz Frequency Range for a Space-Based Radar</b>				
12 PERSONAL AUTHOR(S) <b>Bilow, H.J.</b>				
13a TYPE OF REPORT <b>Interim</b>	13b TIME COVERED FROM _____ TO _____	14 DATE OF REPORT (Year, Month, Day) <b>1984 December 15</b>	15 PAGE COUNT <b>62</b>	
16 SUPPLEMENTARY NOTES				
17 COSATI CODES		18 SUBJECT TERMS (Continue on reverse if necessary and identify by block number)		
FIELD	GROUP	SUB-GROUP		
			Radar Propagation Scintillation Ionosphere	
			Space Troposphere Scattering	
19 ABSTRACT (Continue on reverse if necessary and identify by block number) A survey is made of major phenomena of the lower atmosphere and ionosphere which would introduce clutter and affect propagation in the 0.2-3.0 GHz frequency range in a space-based, ground-looking radar. Attenuation, refractive effects, and weather-related phenomena are included in the study. It is found that the major trade-off that must be made in the frequency range is the relative immunity of the low frequencies to weather related phenomena versus the relative immunity of the high frequencies to deleterious ionospheric effects.				
20 DISTRIBUTION/AVAILABILITY OF ABSTRACT <input checked="" type="checkbox"/> UNCLASSIFIED/UNLIMITED <input type="checkbox"/> SAME AS RPT <input type="checkbox"/> DTIC USERS		21 ABSTRACT SECURITY CLASSIFICATION <b>UNCLASSIFIED</b>		
22a NAME OF RESPONSIBLE INDIVIDUAL <b>H. J. Bilow</b>		22b TELEPHONE (Include Area Code) <b>(202) 767-1047</b>	22c OFFICE SYMBOL <b>Code 5316</b>	

CONTENTS

1. INTRODUCTION..... 1

2. THE LOWER ATMOSPHERE..... 1

    2.1 Refractive Index Effects..... 1

    2.2 Weather Effects..... 5

        2.2.1 Attenuation..... 6

        2.2.2 Scattering..... 14

    2.3 Gaseous Effects..... 19

        2.3.1 Absorption..... 19

        2.3.2 Antenna Temperature..... 23

3. THE IONOSPHERE..... 24

    3.1 Refraction Errors..... 26

    3.2 The Iris Effect..... 30

    3.3 Doppler Errors..... 33

    3.4 Range Errors..... 34

    3.5 Attenuation..... 35

    3.6 Polarization Effects..... 37

    3.7 Scintillation..... 40

4. CONCLUSIONS..... 44

5. REFERENCES..... 44

APPENDIX A. Refraction Error Above the Troposphere or Ionosphere  
in Terms of Error at the Upper Bounding  
Surface of the Medium..... 48

APPENDIX B. Liquid Water Content of Rain-Laden Air..... 52

APPENDIX C. Ionospheric Refraction Error for an Elevated Observer  
in Terms of Refraction Error at the Ground Target... 56

**DTIC**  
**ELECTE**  
**DEC 17 1984**

**B**



iii

Accession For	
NTIS GRA&I	<input checked="" type="checkbox"/>
DTIC TAB	<input type="checkbox"/>
Unannounced	<input type="checkbox"/>
Justification	
By _____	
Distribution/	
Availability Codes	
Dist	Avail and/or Special
A-1	

# PROPAGATION AND SCATTERING CONSIDERATIONS FOR THE 0.2-3.0 GHz FREQUENCY RANGE FOR A SPACE-BASED RADAR

## 1. INTRODUCTION

A space-based, ground-looking radar must contend with a propagation medium characterized by properties that can vary substantially along the path of propagation. In order to realistically predict the performance of such a radar one must be cognizant of the properties of the non-homogeneous propagation path. Since many of these properties are frequency dependent with different properties exhibiting different frequency dependencies, it may be necessary to perform trade-off studies in order to select the optimum frequency with respect to the system requirements and the propagation phenomena.

In the following, a survey is made of the electromagnetic propagation effects associated with the varying properties of the lower atmosphere and ionosphere which are significant for earth-space propagation in the 0.2-3.0 GHz frequency range. The effects of weather-related phenomena are included in the survey.

## 2. THE LOWER ATMOSPHERE

In this section the propagation properties of the portion of the atmosphere below an altitude of 50 km are examined. (Propagation workers often refer to this lower atmospheric region as the troposphere, although in the usual meteorological terminology the troposphere is the portion of the atmosphere extending from ground level to about 10 km in altitude, while the portion of the atmosphere lying between about 10 km and 50 km in height is called the stratosphere ([1], pp. 953, 1040).) The physical phenomena of the lower atmosphere that affect propagation are the gradients in the refractive index, the scattering and absorption of electromagnetic waves by weather-related precipitates and dispersions (rain, snow, clouds, fog), and the absorption and radiation of electromagnetic energy by atmospheric gases. The consequences that these phenomena have for propagation are considered in turn.

### 2.1 Refractive Index Effects

The refractive index of the atmosphere is approximately 1.0003 at sea level and decreases toward unity with increases in altitude. The gradient in the refractive index can cause propagating rays to bend; the perceived direction of a radar target as determined from the refracted rays can thus be different from the actual direction, thereby introducing errors. Doppler errors can also be introduced if the rays between the source and the target propagate along curved rather than straight paths. Finally, range errors can be introduced both by curvature of the ray paths and the non-unity value of the refractive index. Some quantitative results on these effects will now be presented; the angular error will be considered first.

In [2] a graph is exhibited showing the angular error due to refraction when a target in the lower atmosphere is observed from the ground. Employing the data from this graph one finds that the refraction error at the ground,  $\Delta\alpha_G$ , for a target at 100k ft altitude is approximately given by

Manuscript approved August 10, 1984.

$$\Delta\alpha_G(\theta) = \begin{cases} 0.00020 \text{ ctn}\theta \text{ for 100\% humidity} \\ 0.00015 \text{ ctn}\theta \text{ for 0\% humidity} \end{cases} \quad (1)$$

in a standard atmosphere (defined in [1], p. 61) for elevation angle  $\theta$  greater than  $5^\circ$ , where  $\Delta\alpha_G$  is in radians. In the case of interest here the observer would be elevated and the target near the ground, so that this formula cannot be applied directly. However, by using a formula for the total bending  $\tau$  of a ray propagating through the lower atmosphere ([3], p. 24-5)

$$\tau = (n_G - 1) \text{ctn}\theta$$

where  $n_G$  is the refractive index at the ground (where the target is assumed to be located), and by noting that (see Fig. 1)

$$\tau = \Delta\alpha_G + \Delta\alpha_0$$

where  $\Delta\alpha_0$  is the angular error as seen by the elevated observer, one finds that

$$\Delta\alpha_0 = \tau - \Delta\alpha_G,$$

or

$$\Delta\alpha_0(\theta) = \begin{cases} (n_G - 1.00020) \text{ctn}\theta \text{ for 100\% humidity} \\ (n_G - 1.00015) \text{ctn}\theta \text{ for 0\% humidity} \end{cases} \quad (2)$$

If one employs the values, obtained from formulas in [2] at zero altitude, of  $n_G = 1.000338$  and  $1.000262$  for 100% and 0% relative humidity, respectively, then Eq. (2) becomes

$$\Delta\alpha_0(\theta) = \begin{cases} 0.000138 \text{ ctn}\theta \text{ for 100\% humidity} \\ 0.000112 \text{ ctn}\theta \text{ for 0\% humidity} \end{cases} \quad (3)$$

At  $\theta = 5^\circ$ , the minimum elevation for which Eq. (3) is valid, one obtains a value of 1.6 milliradians for  $\Delta\alpha_0$  for 100% humidity. For higher elevation angles or for lower humidity the angular error will be less.

Eq. (3) applies when the observer is at an altitude of 100k ft. Since the interest here is on space applications in which the observer would be many times this altitude, a formula more appropriate for current needs is required. If  $\Delta\alpha$  represents the angular error for observations of the ground, then it is shown in Appendix A that

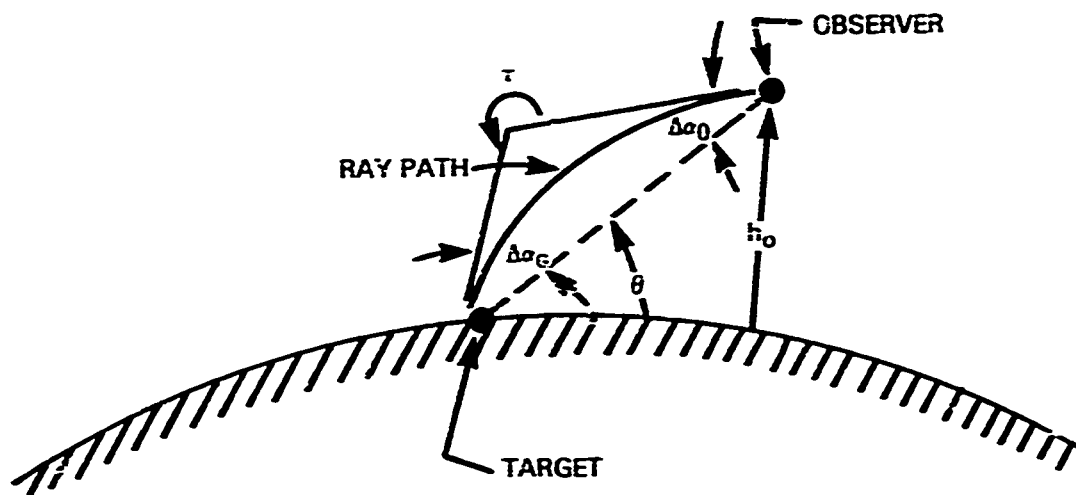


Fig. 1 - Geometry of angular errors and ray bending.

$$\Delta\alpha(h, \theta) = \Delta\alpha_0(\theta) \left[ \frac{[\sin^2\theta + 2(h_0/r_0) + (h_0/r_0)^2]^{1/2} - \sin\theta}{[\sin^2\theta + 2(h/r_0) + (h/r_0)^2]^{1/2} - \sin\theta} \right] \quad (4)$$

where  $h_0 = 100k$  ft, where  $h$  is the altitude of the observer ( $h > h_0$ ), and where  $r_0$  is the radius of the earth. The angular error  $\Delta\alpha$  is seen to decrease as the observer's altitude increases with  $\theta$  remaining constant. In terms of the straight line distance  $D(h, \theta)$  between the target and the observer one obtains

$$\Delta\alpha(h, \theta) = \frac{D(h_0, \theta)}{D(h, \theta)} \Delta\alpha_0(\theta). \quad (5)$$

It can be seen from this last formula that the error in the calculated position of the target on the ground due to refraction, proportional to  $\Delta\alpha(h, \theta) \times D(h, \theta)$ , will remain constant as the altitude increases for a constant elevation angle.

Eqs. (4) and (5) are derived on the assumption that the index of refraction is unity above 100k ft; the ionosphere is not taken into account. The equations allow one to gauge the magnitude of the angular error caused by refraction in the lower atmosphere, even when ionospheric refraction is present.

Results for the effect of refraction in the lower atmosphere on the doppler frequency will now be given. The problem was dealt with in [2] for the case in which the observer was fixed on the ground and the moving target was elevated. The results given by Eq. (39) in [2] can be applied to the current problem by replacing  $\Delta\alpha_T$  with  $\Delta\alpha_G$  so that one has

$$\Delta f_d = - \frac{2fV}{c} \Delta\alpha_G(\theta) \cos\psi \sin\theta .$$

Here  $f$  is the r.f. frequency of the radar,  $c$  is the speed of light,  $\Delta f_d$  is the refraction-induced doppler error, and  $V$  is interpreted as the total relative velocity of the target with respect to the observer (the observer, a satellite, will be in motion). The quantity  $\psi$  is the angle between the (relative) velocity vector of the target and the straight line drawn from the observer to the target; the  $\cos\psi$  factor was mistakenly dropped in [2]. Since the doppler frequency  $f_d$  is given by

$$f_d = - \frac{2fV}{c} \cos\psi ,$$

one sees that

$$\frac{\Delta f_c}{f_c} = \Delta \alpha_G(\theta) \sin \psi \quad (6)$$

Substituting the expression for  $\Delta \alpha_G$  given by Eq. (1) into Eq. (6), one obtains

$$\frac{\Delta f_c}{f_c} = \begin{cases} 0.00020 \text{ctn} \theta \sin \psi & \text{for 100\% humidity} \\ 0.00015 \text{ctn} \theta \sin \psi & \text{for 0\% humidity.} \end{cases} \quad (7)$$

At  $\theta = 5^\circ$ , the lowest elevation angle for which Eq. (7) can be employed, the relative doppler error is found to be 0.23% near  $\psi = 90^\circ$  for 100% humidity. At higher elevation angles or at lesser angles between the velocity vector and the observer-to-target line the error will be less.

The range errors introduced by refraction and propagation velocity changes in the lower atmosphere can also be found in [2]. A formula which gives a reasonably good fit to the graphical data in the reference for an observer at an altitude of at least 100k ft is

$$\Delta D(\theta) = \begin{cases} 3.3 \text{ csc} \theta & \text{for 100\% humidity} \\ 7.3 \text{ csc} \theta & \text{for 0\% humidity,} \end{cases} \quad (8)$$

$\Delta D$  being the one-way range error in feet when the observer is at elevation angle  $\theta$ . This formula will tend to break down for elevation angles below  $5^\circ$ .

As an example of the type of errors observed, the Eq. (8) gives a value of 95.2 feet for the one-way range error at  $5^\circ$  elevation and 100% humidity.

The effects described in this section are frequency independent. In the following sections frequency dependent effects will be discussed.

## 2.2 Weather Effects

The effects of certain weather phenomena on the propagation of electromagnetic waves in the frequency range of interest will now be considered. In particular, the effects of rain, hail, snow, clouds and fog will be examined.

The physical processes by which these phenomena affect propagating waves are absorption and scattering. In general, waves propagating through an atmosphere in which these phenomena are present will be attenuated by both absorption and scattering. However, in the frequency range of interest here the wavelength (a minimum of 10 cm) is much greater than the linear dimensions of any of the associated particles (raindrops, fog droplets, etc.) and attenuation due to scattering is insignificant in comparison to that due to absorption ([4], pp. 672-673). Nevertheless, scattering cannot be ignored since the energy reflected back to the observer may constitute a significant amount of clutter.

## 2.2.1 Attenuation

### (i) Rain

Attenuation by rain will be the first topic to be considered here. A formula which has been found useful in estimating this attenuation is [5]

$$A = aR^b \quad (9)$$

where

$$a = \begin{cases} 6.39 \times 10^{-5} f_{\text{GHz}}^{2.03} & , f_{\text{GHz}} < 2.9 \\ 4.21 \times 10^{-5} f_{\text{GHz}}^{2.42} & , 2.9 < f_{\text{GHz}} < 5.4 \end{cases}$$

$$b = 0.851 f_{\text{GHz}}^{0.158} \quad , f_{\text{GHz}} < 8.5 .$$

A is the one-way attenuation in dB/km, R is the rain rate in mm/hr, and  $f_{\text{GHz}}$  is the frequency of propagation in GHz. The values of a and b furnished with Eq. (9) apply to rain at a temperature of 0°C; the effect of temperature on attenuation will be discussed shortly. Table 1 provides values of A for a range of rain rates and frequencies. The attenuation is seen to increase approximately as the square of the frequency.

The values in Table 1 apply to rain at a temperature of 0°C. Attenuation will decrease with increasing temperature, and since changes of 3 to 1 can be observed over a 40°C temperature span, a correction formula for temperature is desirable. If the attenuation is principally due to absorption, a reasonable assumption in the present frequency range, then the attenuation is governed by the equation ([3], p. 24-22)

$$A = -8.186 M \lambda_{\text{cm}}^{-1} \text{Im} \left\{ (\epsilon_w - 1) / (\epsilon_w + 2) \right\} \quad (10)$$

where A is again the attenuation in dB/km, M the liquid water content of air in  $\text{g/m}^3$  (a plot of M versus rain rate is given in Appendix B),  $\lambda_{\text{cm}}$  the wavelength in cm of the propagating wave, and  $\epsilon_w$  is the complex relative dielectric constant of water. By using the Debye formula for  $\epsilon_w$  which appears in [4], p. 675, with some slight notational changes, viz.,

$$\epsilon_w = \frac{\epsilon_{w0} - \epsilon_{w\infty}}{1 + i \frac{\Delta\lambda}{\lambda_{\text{cm}}}} + \epsilon_{w\infty} \quad (11)$$

where  $\epsilon_{w0}$ ,  $\epsilon_{w\infty}$ , and  $\Delta\lambda$  are temperature dependent constants, and by taking note of the facts that  $\epsilon_{w0} \gg \epsilon_{w\infty}$  and  $\Delta\lambda \ll \lambda_{\text{cm}}$  in the current frequency range (which can be seen from the tabulations in [4], p. 675), one can show that

TABLE 1. Attenuation in dB/km for Various Rain Rates and Frequencies for Temperature of 0°C

		R (mm/hr)										
		0.25	1.25	2.5	5.0	12.5	25.0	50.0	100.	150.	200.	
f GHz	0.2	$9.76 \times 10^{-7}$	$2.82 \times 10^{-6}$	$4.46 \times 10^{-6}$	$7.05 \times 10^{-6}$	$1.29 \times 10^{-5}$	$2.04 \times 10^{-5}$	$3.22 \times 10^{-5}$	$5.09 \times 10^{-5}$	$6.65 \times 10^{-5}$	$8.04 \times 10^{-5}$	
	0.5	$5.44 \times 10^{-6}$	$1.86 \times 10^{-5}$	$3.15 \times 10^{-5}$	$5.34 \times 10^{-5}$	$1.07 \times 10^{-4}$	$1.82 \times 10^{-4}$	$3.09 \times 10^{-4}$	$5.25 \times 10^{-4}$	$7.15 \times 10^{-4}$	$8.90 \times 10^{-4}$	
	1.0	$1.96 \times 10^{-5}$	$7.73 \times 10^{-5}$	$.000139$	$.000251$	$.000548$	$.000989$	$.00178$	$.00322$	$.00454$	$.00580$	
	2.0	$7.00 \times 10^{-5}$	$.000323$	$.000623$	$.00120$	$.00287$	$.00555$	$.0107$	$.0207$	$.0304$	$.0399$	
	3.0	$.000146$	$.000745$	$.00150$	$.00303$	$.00766$	$.0155$	$.0312$	$.0629$	$.0948$	$.127$	

$$\operatorname{Im}\left\{\frac{\epsilon_w-1}{\epsilon_w+2}\right\} \equiv -\frac{1}{\lambda_{\text{cm}}}\frac{3(\epsilon_{w0}-\epsilon_{w\infty})\Delta\lambda}{(\epsilon_{w0}+2)} \quad (12)$$

Let  $K_i(T, \lambda_{\text{cm}})$  denote the expression on the left-hand side of Eq. (12) with its implicit temperature dependence, i.e.,

$$K_i(T, \lambda_{\text{cm}}) \equiv \operatorname{Im}\left\{\frac{\epsilon_w-1}{\epsilon_w+2}\right\} \quad (13)$$

Then by substituting the tabulated values of  $\Delta\lambda$ , etc. ([4], p. 675, where the decimal point is in error in the 30° and 40° values for  $\Delta\lambda$ ) into the right-hand side of Eq. (12) one can obtain the values given in Table 2. It can be seen from Eq. (12) that the quantity  $\lambda_{\text{cm}}K_i$  which appears in the table is independent of  $\lambda_{\text{cm}}$ . The tabulated ratio  $K_i(T, \lambda_{\text{cm}})/K_i(0, \lambda_{\text{cm}})$  is the temperature correction factor, i.e., the factor by which one multiplies the 0°C attenuation (in dB) in order to obtain the attenuation at temperature T. This factor can also be seen to be independent of  $\lambda_{\text{cm}}$ . It should be noted that the  $\lambda$ -independence observed here would not be valid for wavelengths much less than the minimum wavelengths of current concern (10 cm). Finally, it is noted that some of the values shown in Table 2 differ by a few percent from those calculated by Gunn and East ([6], Table 1).

TABLE 2. Temperature Dependence of Water Absorption Factor and Attenuation Correction Factor

T (°C)	$\lambda_{\text{cm}}K_i(T, \lambda_{\text{cm}})$	$K_i(T, \lambda_{\text{cm}})/K_i(0, \lambda_{\text{cm}})$
0	-0.110	1.0
10	-0.0713	0.65
18	-0.0546	0.50
20	-0.0509	0.46
30	-0.0388	0.35
40	-0.0309	0.28

Eq. (9) and Table 1 give the one-way rain attenuation per km. Rain models have also been developed for predicting the total one-way attenuation in rain for various rain rates and for various elevation angles of the source. One of these models is that of Lin as given in [7]:

$$A_t = aR_5^b \left[ \frac{2636}{R_5 - 6.2 + \frac{2636 \sin \theta}{4 - G}} \right] \quad (14)$$

Here  $A_t$  is the total one-way loss in dB,  $R_5$  is the five-minute average rain-rate in mm/h,  $G$  is the elevation of the ground above sea level in km, and  $\theta$  is the elevation of the source. Quantities  $a$  and  $b$  are the same as those given with Eq. (9).

Plots of the total one-way attenuation versus rain rate for several frequencies are given in Fig. 2.

This section on rain attenuation is concluded with Fig. 3 and accompanying Table 3 (both taken from [7]) which show the U.S. and global distribution of rain employed in another rain attenuation model, the Crane model.

TABLE 3 - Point Rain Distribution Values (mm/h) versus Percent of Year Rain Rate Is Exceeded (from [7])

Rain rate exceeded, percent of year	Point rain rate distribution values (mm/hr) per rain climate region										Minutes per year	Hours per year
	A	B	C	D <sub>1</sub>	D <sub>2</sub>	D <sub>3</sub>	E	F	G	H		
0.001	28	54	90	90	102	127	164	64	129	251	2.3	0.09
.002	24	40	62	72	96	107	144	51	109	220	19.5	.18
.005	19	26	41	50	64	81	117	34	85	178	23	.44
.01	15	19	28	37	49	63	98	23	67	147	53	.88
.02	12	14	18	27	35	46	77	14	51	115	105	1.75
.05	8	9.5	11	16	22	31	52	8.0	33	77	263	4.38
.1	6.5	6.8	7.2	11	15	22	35	5.5	22	51	526	8.77
.2	4.0	4.8	4.8	7.5	9.5	14	21	3.8	14	31	1052	17.5
.5	2.5	2.7	2.8	4.0	5.2	7.0	8.5	2.4	7.0	13	2430	40.5
1.0	1.7	1.8	1.9	2.2	3.0	4.0	4.0	1.7	3.7	6.4	5260	87.66
2.0	1.1	1.2	1.2	1.5	1.8	2.5	2.0	1.1	1.6	2.8	10520	175.3

(ii) Snow

A formula for the attenuation of electromagnetic waves propagating in falling snow is given by Gunn and East ([6], p. 536). In the frequency range of interest here only the second term of the attenuation expression is significant, allowing one to obtain

$$A = 0.00224R/\lambda_{cm} \quad (15)$$

for the one-way attenuation  $A$  in dB/km at 0°C where the rate at which the snow falls is equivalent to liquid water fall rate of  $R$  mm/h. (As a rule of thumb, the liquid water rate is 1/10 the snow fall rate ([1], p. 863).) A tabulation of attenuation for several values of  $R$  and frequency is given in Table 4. Attenuation in snow is proportional to frequency in the present frequency range, whereas it may be recalled that rain attenuation tends to vary with the square of the frequency.

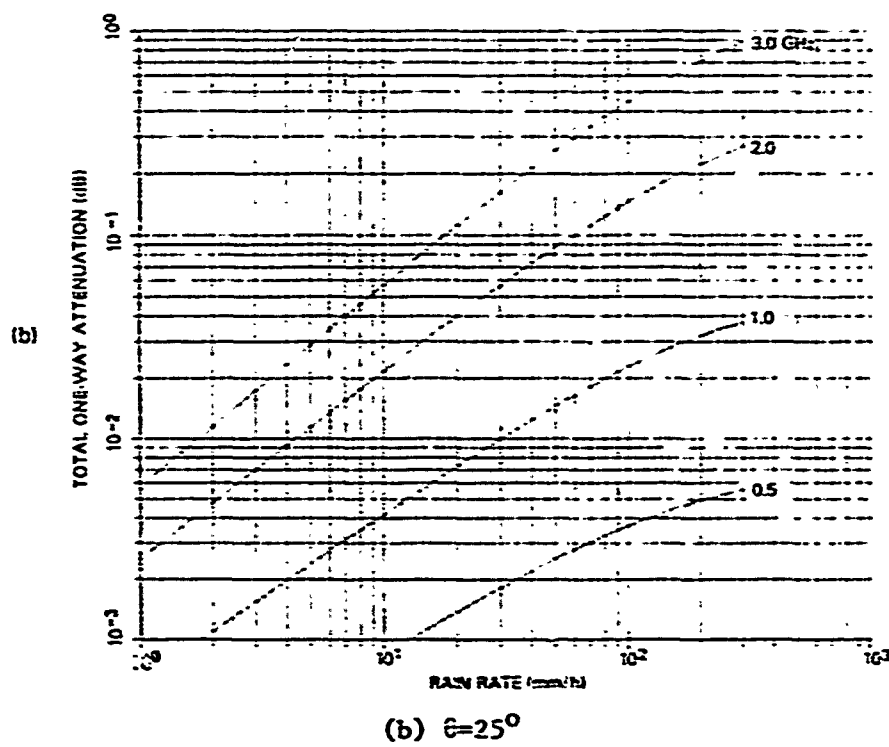
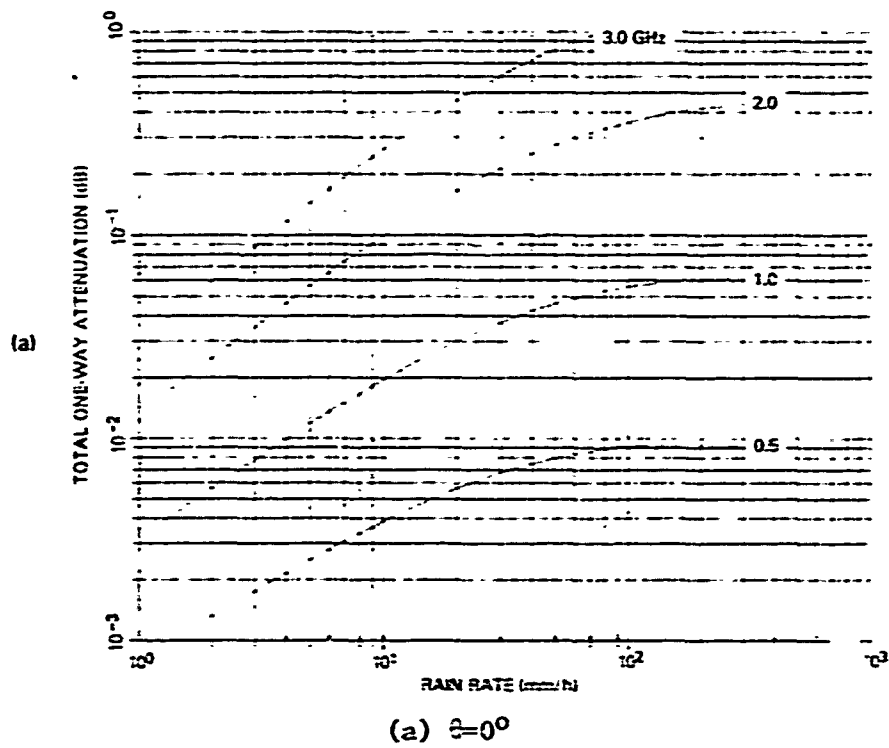


Fig. 2 - Total one-way attenuation in rain for several elevation angles.

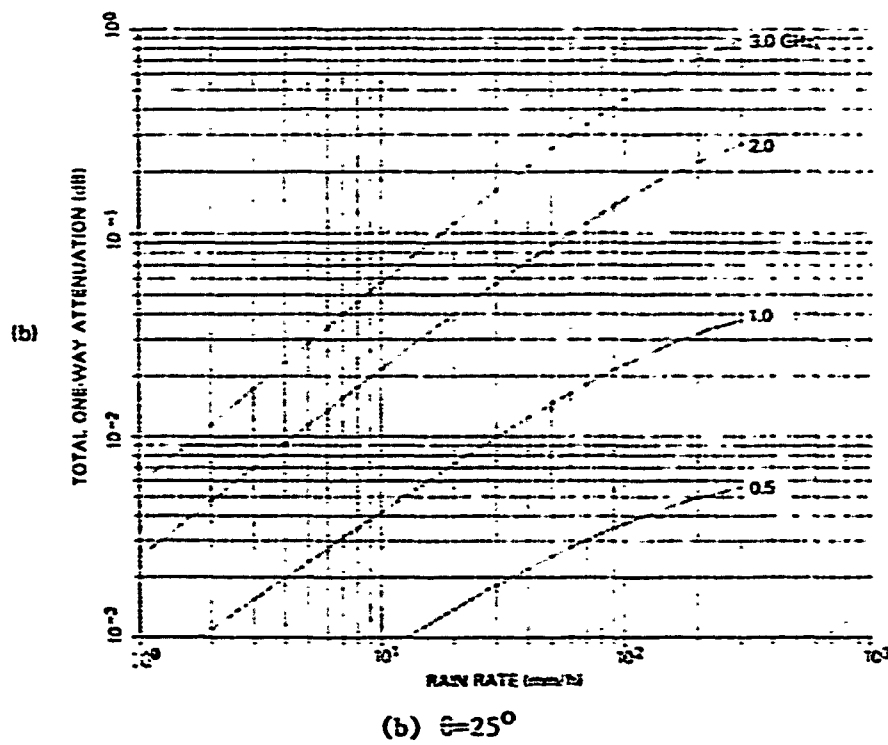
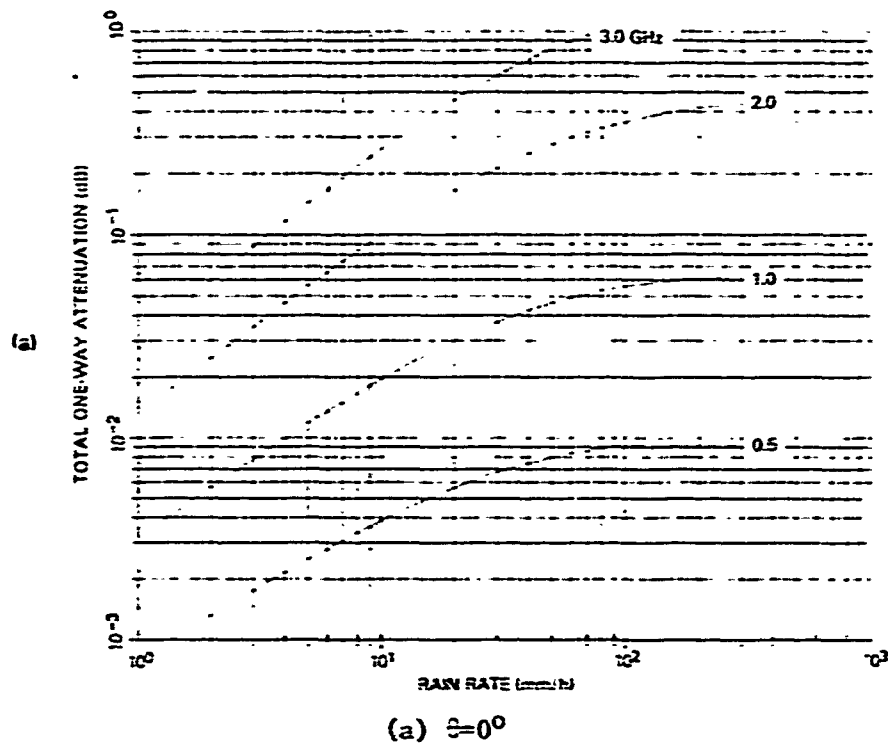


Fig. 2 - Total one-way attenuation in rain for several elevation angles.

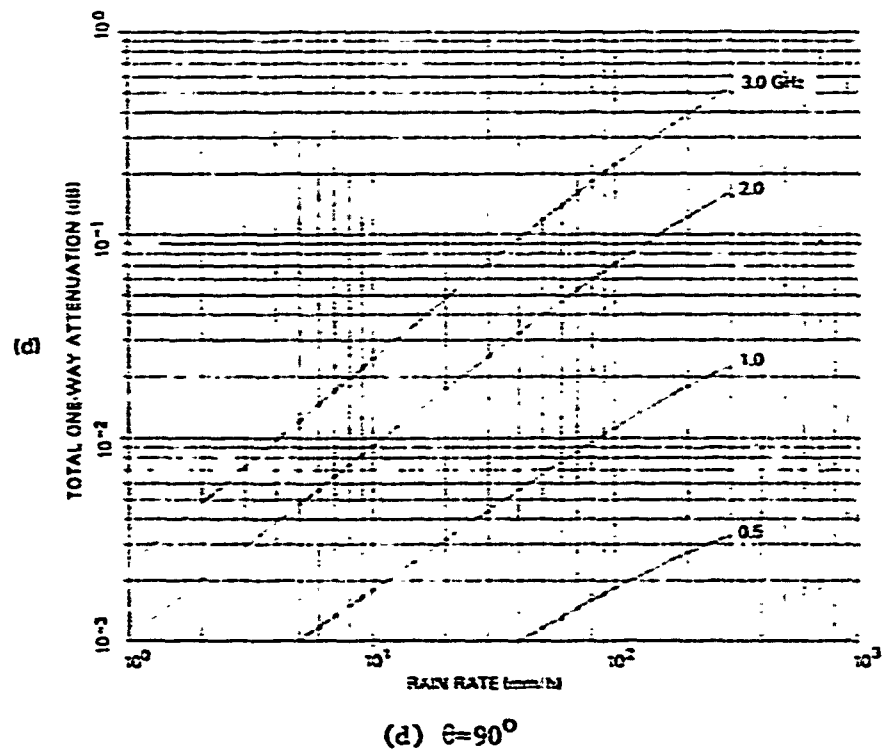
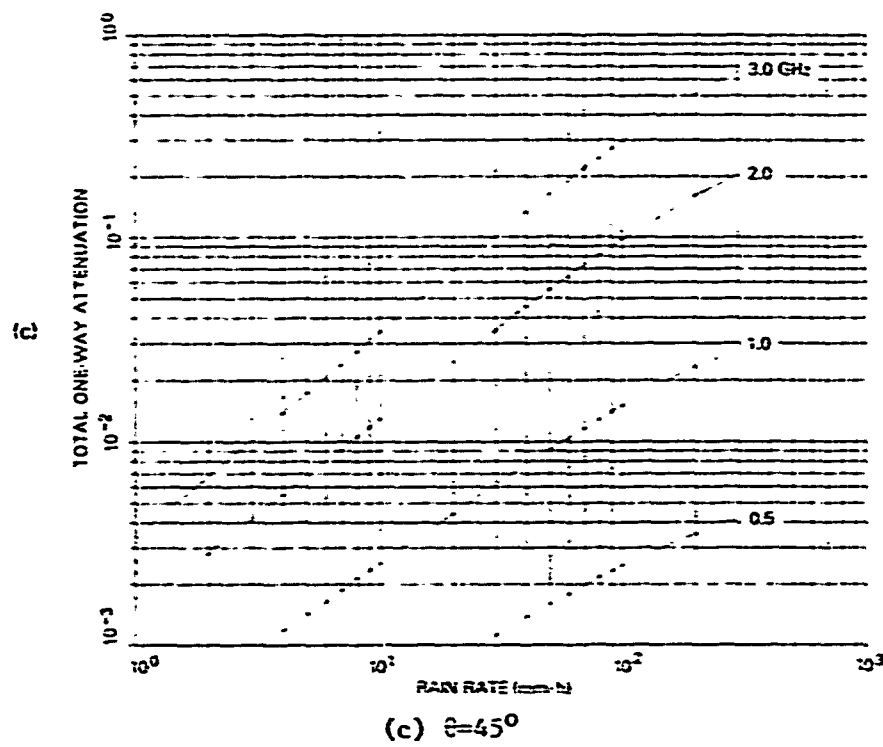
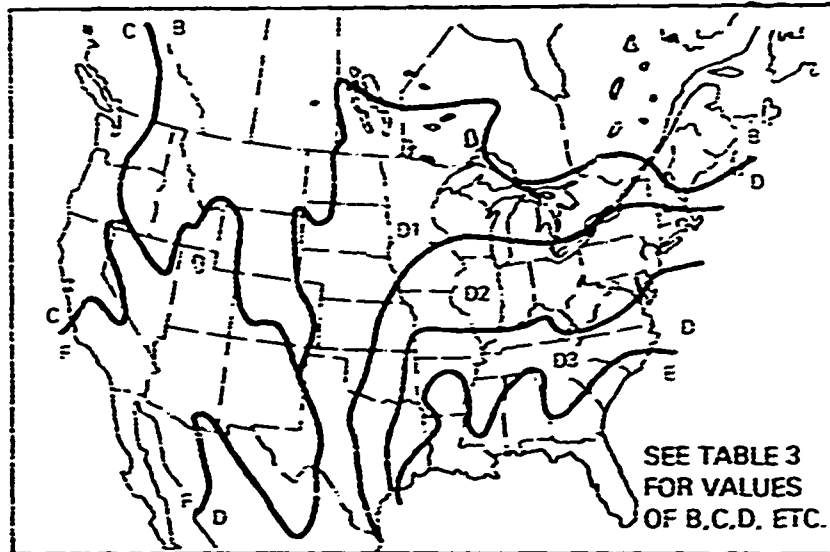
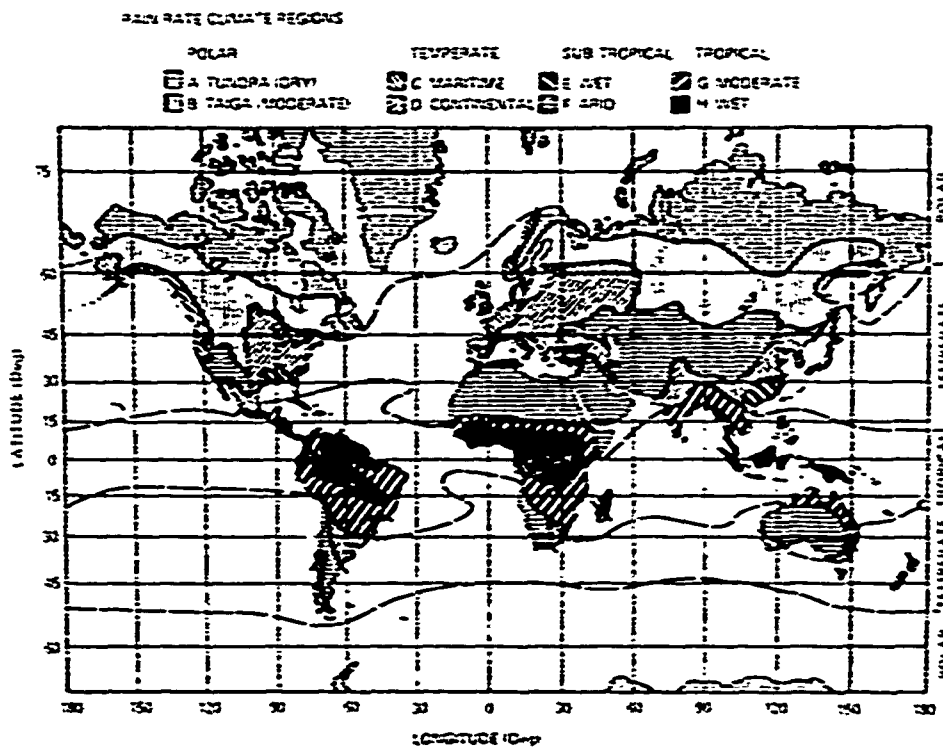


Fig. 2 (Cont'd) - Total one-way attenuation in rain for several elevation angles.



(a) Continental U.S.



(b) Global (from [7])

Fig. 3 - Rain rate climate regions.

TABLE 4 - One-Way Attenuation in Snow (dB/km)

$f$ GHz	R (mm/h of Liquid Water)					
	0.25	1.25	2.5	1.5	10.	2.5
0.2	$3.7 \times 10^{-6}$	$1.9 \times 10^{-5}$	$3.7 \times 10^{-5}$	$7.5 \times 10^{-5}$	$1.5 \times 10^{-4}$	$3.7 \times 10^{-4}$
0.5	$9.3 \times 10^{-6}$	$4.7 \times 10^{-5}$	$9.3 \times 10^{-5}$	$1.9 \times 10^{-4}$	$3.7 \times 10^{-4}$	$9.3 \times 10^{-4}$
1.0	$1.9 \times 10^{-5}$	$9.3 \times 10^{-5}$	$1.9 \times 10^{-4}$	$3.7 \times 10^{-4}$	$7.5 \times 10^{-4}$	0.0019
2.0	$3.7 \times 10^{-5}$	$1.9 \times 10^{-4}$	$3.7 \times 10^{-4}$	$7.5 \times 10^{-4}$	0.0015	0.0037
3.0	$5.6 \times 10^{-5}$	$2.8 \times 10^{-4}$	$5.6 \times 10^{-4}$	0.0011	0.0022	0.0056

As with rain, attenuation in snow exhibits a temperature dependence. The attenuation in snow tends to decrease with decreases in temperature, however. The attenuation will be given by Eq. (10) if one replaces  $\epsilon_w$  with  $\epsilon_i$ , the complex relative dielectric constant of ice. It is convenient to define an absorption factor  $\tilde{\kappa}_i$  for ice analogous to the  $\tilde{\kappa}_w$  factor defined for liquid water in (13). In particular one defines

$$\tilde{\kappa}_i(T) \equiv \text{Im} \left[ \frac{\epsilon_i - 1}{\epsilon_i + 2} \right] \quad (16)$$

Values for  $\tilde{\kappa}_i$  are given in [6] (Table 2, p. 525). One can employ these values to obtain the temperature correction factor  $\tilde{\kappa}_i(T)/\tilde{\kappa}_i(0)$  for several values of T; the values of the factor are given in Table 5.

The values of  $\tilde{\kappa}_i$  from which the temperature correction factors of Table 5 were computed were actually determined from measurements in the 3 cm to 9 cm band. However, it appears likely that the tabulated values of the factors apply to the entire wavelength span of interest here (10 cm to 150 cm) for the following reasons. The data in [8] indicate that the Debye formula, which has the form given in Eq. (11), adequately characterizes the dielectric properties of ice when  $\Delta\lambda$  is a temperature dependent parameter assuming values of from 6.6 km to 49 km in the  $-0.1^\circ\text{C}$  to  $-21^\circ\text{C}$  temperature range. Then because the  $\Delta\lambda$  parameter is much greater than the maximum wavelength of interest (150 cm), the Debye formula shows that the dielectric properties of ice will exhibit little variation across the entire band of interest as well as at even shorter wavelengths. The wavelength invariance of the measured dielectric properties of ice in the 3 cm to 9 cm band tends to indicate that this is indeed the case.

### (iii) Hail

The attenuation properties of hail would tend to be extremely variable, assuming that the individual hailstones would generally have a liquid water coating. This can be inferred from the finding that the absorption in an ice sphere surrounded by a spherical liquid water shell can vary

from a small fraction of the absorption that would be exhibited by a water sphere of the same total mass to more than twice that of the water sphere, depending on the thickness of the liquid water shell [6].

(iv) Clouds and Fog

Attenuation in fog and liquid water clouds, where the droplet size is on the order of 0.01 cm or less ([3], p. 24-22 and [4], p. 677), is given by Eq. (10) with the aid of definition (13) and Table 2. The value of  $M$ ,

TABLE 5. Temperature Dependence of Ice Absorption Factor and Attenuation Correction Factor

T(°C)	$K_i(T)$	$K_i(T)/K_i(0)$
0	$-9.6 \times 10^{-4}$	1.0
-10	$-3.2 \times 10^{-4}$	0.33
-20	$-2.2 \times 10^{-4}$	0.23

the liquid water content, varies from 1 to 2.5 g/m<sup>3</sup> in clouds, although values as high as 4 g/m<sup>3</sup> have been observed ([3], p. 24-22); in fog  $M$  is typically much less than 1 g/m<sup>3</sup> although values as high as 2.3 g/m<sup>3</sup> may be found in heavy sea fogs ([4], pp. 677, 683).

Eq. (10) can be employed to obtain the attenuation in ice clouds by replacing  $\epsilon_w$  with  $\epsilon_i$  and by using definition (16) and Table 5. The values of attenuation obtained apply to ice crystals uncoated by liquid water; a water coating will cause the type of variability in attenuation noted for hail. The mass of ice per unit volume of air in ice clouds tends to be substantially less than the mass of water found in liquid water clouds, often being less than 0.1 g/m<sup>3</sup> and rarely more than 0.5 g/m<sup>3</sup> ([6], p. 24-22).

Plots of attenuation in fog and clouds at 0°C are displayed in Fig. 4. Attenuation at other temperatures can be obtained by multiplying the attenuation obtained from this figure by the value in the third column of Table 2 (for liquid water) or Table 5 (for ice) corresponding to the desired temperature.

2.2.2 Scattering

All of the weather phenomena considered in the section on attenuation will reflect electromagnetic energy back towards the source. This energy may constitute a significant amount of clutter.

For collections of particles whose diameters are much less than the wavelength of the scattered wave, as will be the case here, the scattering cross-section  $\eta$  in square meters per cubic meter of the particle-filled medium is ([3], p. 24-22)

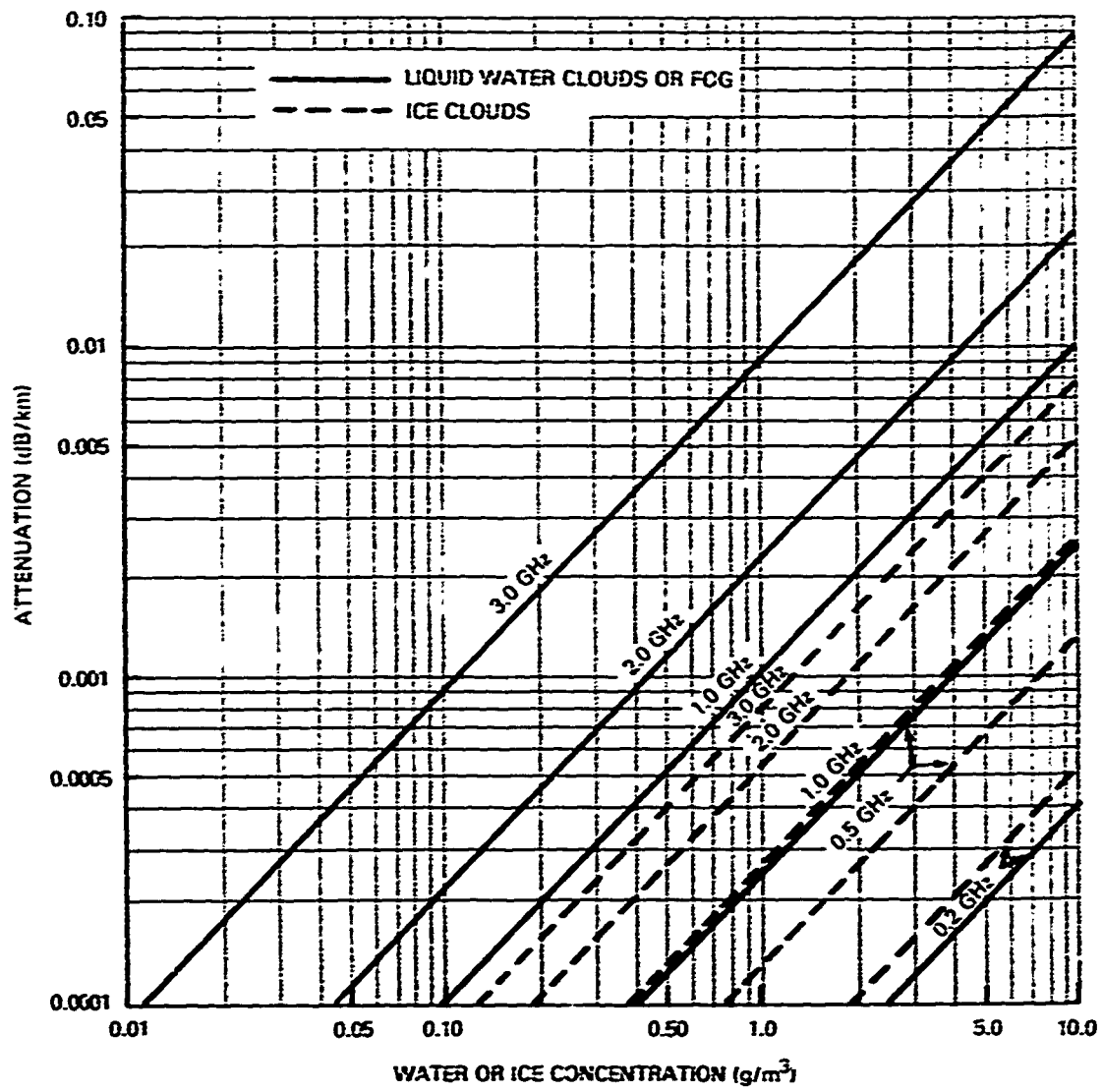


Fig. 4 - One-way attenuation in fog and clouds at 0° C.

$$\eta = 10^{-10} \frac{5}{\lambda_{\text{cm}}^5} |K|^2 Z \quad (17)$$

where

$$K \equiv \frac{\epsilon - 1}{\epsilon + 2},$$

$\epsilon$  being the complex relative dielectric constant of the particle scatterers, and where  $Z$  is the reflectivity factor in units of millimeters to the sixth power per cubic meter, values for which will be given shortly. The factor  $10^{-10}$  which appears in (17) but not in [3] arises from the units selected here for  $\eta$  and the wavelength.

The factor  $|K|^2$  which appears in Eq. (17) is relatively insensitive to both temperature and frequency for water and ice, as a study of Tables 1 and 2 in [6] reveals. One can simply employ the values

$$|K|^2 = \begin{cases} 0.93 & \text{for liquid water} \\ 0.21 & \text{for ice} \end{cases} \quad (18)$$

independently of temperature and frequency.

The reflectivity factors for the weather phenomena of interest here are ([3], pp. 24-31, 24-32)

$$Z = \begin{cases} 200 R^{1.6} & \text{for rain} \\ 1000 R^{1.6} & \text{for snow} \\ 4.8 \times 10^{-2} M^2 & \text{for fog and liquid water clouds} \end{cases} \quad (19)$$

where  $Z$  is in units of  $(\text{mm})^6/\text{m}^3$ , where  $R$  is the rain rate (or equivalent rain rate for snow) in  $\text{mm}/\text{h}$ , and where  $M$  is the mass of liquid water per unit volume of air in  $\text{g}/\text{m}^3$ .

A plot of the volumetric reflectivity (scattering cross-section per unit volume) for rain and snow is shown in Fig. 5, while Fig. 6 shows the corresponding plot for fog and liquid water clouds.

The scattering cross-section of hail should be strongly dependent on the relative thickness of the water coating the hailstone is likely to have. This is due to the fact that the scattering cross-section of a spherical drop of liquid water is factor 4.3 greater than the cross-section of the same drop when completely frozen; a partially frozen drop of water consisting of a spherical particle of ice surrounded by a spherical shell of liquid water has a scattering cross-section which exceeds that of the completely frozen drop by a factor between unity and 4.3, depending on the relative masses of ice and liquid water [6].

The reflectivity factor  $Z$  for an ice cloud will be the same as that

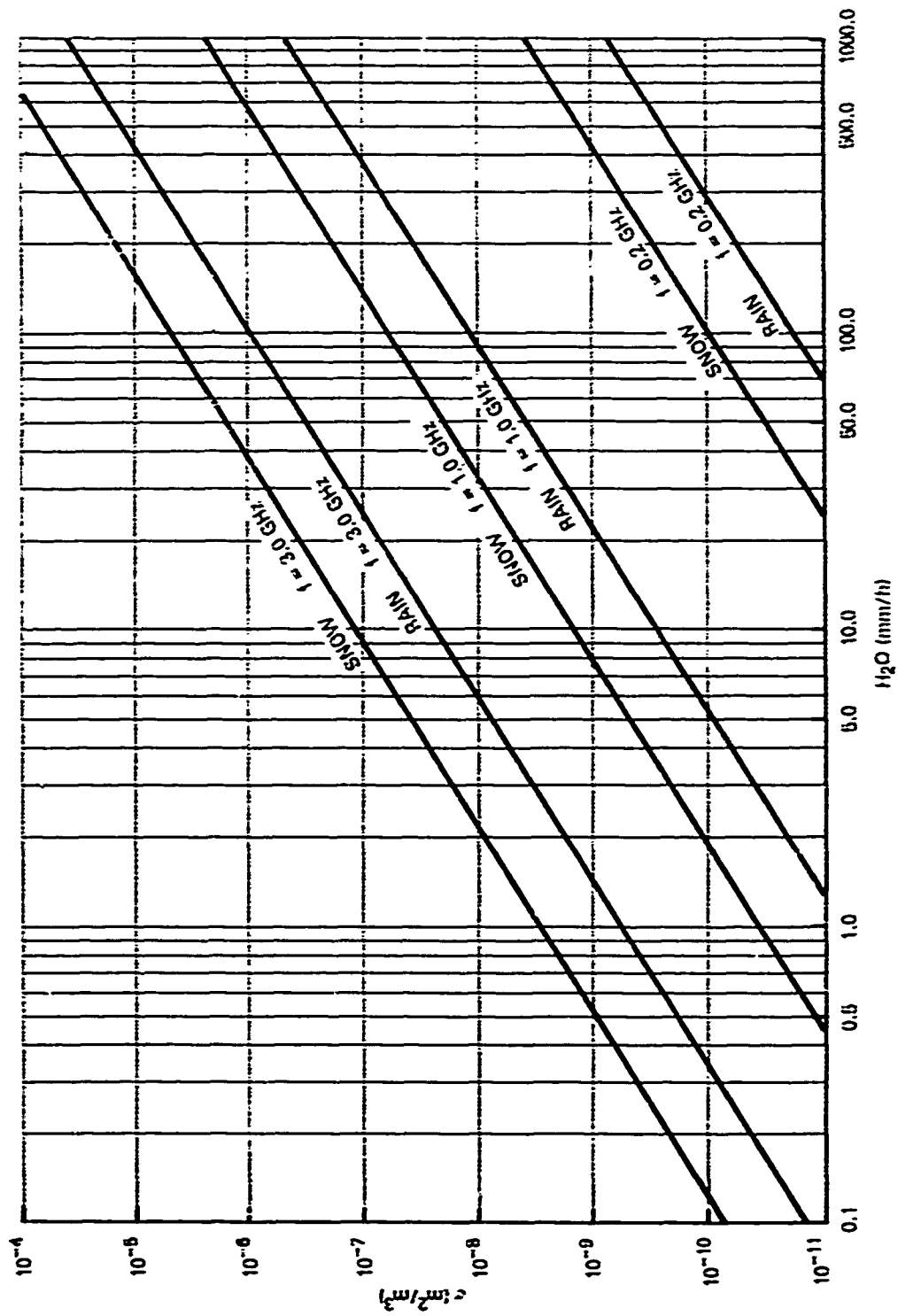


Fig. 5 - Volumetric scattering for rain and snow.

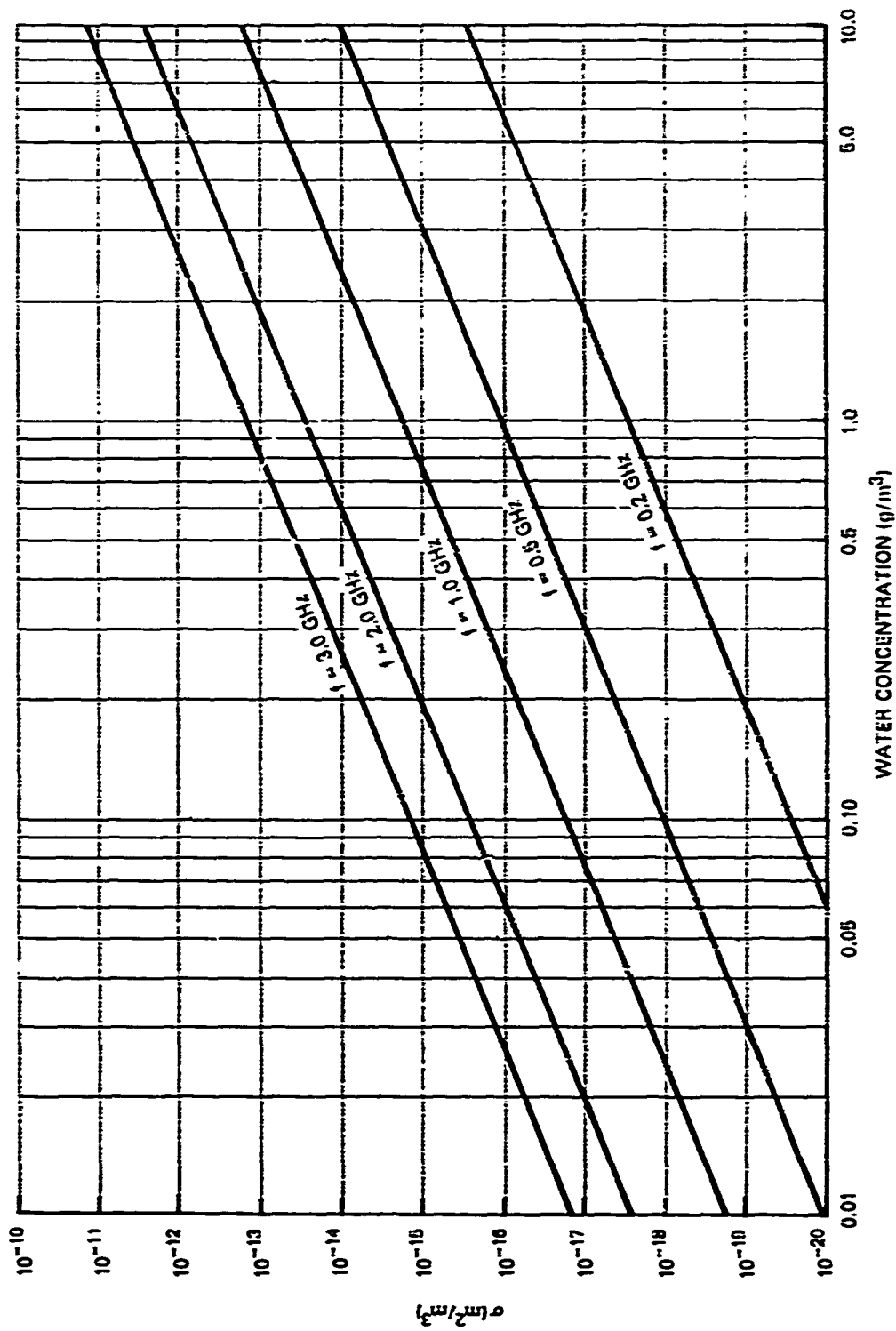


Fig. 6 - Volumetric scattering for fog and liquid water clouds.

for a liquid water cloud if the relative distribution of particle diameters is the same. In this case the reflectivity of the ice cloud will be about 0.23 the reflectivity of the liquid water cloud by virtue of the ratio of the values of  $|K|^2$  for ice and liquid water (Eq. (18)), assuming that the ice crystals do not have appreciable liquid water coatings. Liquid water coatings would cause the same type of variation in cross-section that was noted in connection with hail.

## 2.3 Gaseous Effects

### 2.3.1 Absorption

The oxygen molecule possesses a magnetic dipole moment which causes gaseous oxygen to undergo an energy-absorbing interaction with any time-varying electromagnetic field that may be present; similarly, the water molecule possesses an electric dipole moment which likewise causes water vapor to undergo an energy-absorbing interaction with a time varying field ([4], pp. 648-664; [3], pp. 24-13, 24-14; [6]; [7]). As a result of these interactions, an electromagnetic wave will suffer attenuation as it propagates through the atmosphere.

The absorption in dB/km at sea level (1013 mb atmospheric pressure) and at 68°F can be obtained from ([3], pp. 24-13, 24-14)

$$\alpha_{O_2} = \frac{0.34}{\lambda^2_{cm}} \left[ \frac{\Delta v_1/c}{1/\lambda^2_{cm} + (\Delta v_1/c)^2} + \frac{\Delta v_2/c}{(1/\lambda_{cm} - 2)^2 + (\Delta v_2/c)^2} + \frac{\Delta v_2/c}{(1/\lambda_{cm} + 2)^2 + (\Delta v_2/c)^2} \right] \quad (20)$$

$$\alpha_{H_2O} = \frac{\rho_v}{\lambda^2_{cm}} \left\{ 0.035 \left[ \frac{\Delta v_3/c}{(1/\lambda_{cm} - 1/1.35)^2 + (\Delta v_3/c)^2} + \frac{\Delta v_3/c}{(1/\lambda_{cm} + 1/1.35)^2 + (\Delta v_3/c)^2} \right] + 0.05(\Delta v_4/c) \right\} \quad (21)$$

where  $\alpha_{O_2}$  and  $\alpha_{H_2O}$  are the absorption coefficients for oxygen and water vapor, respectively, where

$$\Delta v_1/c = 0.018,$$

$$\Delta v_2/c = 0.050,$$

$$\Delta v_3/c = \Delta v_4/c = 0.0906,$$

and where  $\rho_v$  is the absolute humidity in grams (of water vapor) per cubic meter of air.

A number of values calculated with the aid of Eqs. (20) and (21) are given in Table 6. Table 7, adapted from [1], p. 444, gives values of  $\rho_v$  in saturated air (100% of relative humidity) at 1013 mb atmospheric pressure for a range of temperatures; a plot of these values is shown in Fig. 7. The attenuation at sea level due to water vapor is given approximately by the value of  $\lambda_{H_2O}/\rho_v$  taken from Table 6 times the value of  $\rho_v$  taken

from Table 7 (or Fig. 7) times the relative humidity divided by 100%. In order to obtain more exact values for  $\lambda_{H_2O}$  or  $\lambda_{O_2}$  at other temperatures or

pressures, one must employ correction factors for the  $\Delta v/c$  values and the coefficients used in Eqs. (20) and (21) (see [3], pp. 24-14, 24-15, 24-16).

TABLE 6. One-way Attenuation in  $O_2$  and in Water Vapor (per gram of water vapor per  $m^3$ ) at Sea Level (1013 mb) and at 68° F.

$f_{GH_2}$	$\lambda_{O_2}$ (dB/km)	$\lambda_{H_2O}/\rho_v$ (dB/km per $g/m^3$ )
0.2	0.00074	0.00000025
0.3	0.0014	0.00000057
0.4	0.0022	0.0000010
0.5	0.0029	0.0000016
0.6	0.0034	0.0000023
0.8	0.0042	0.0000040
1.0	0.0047	0.0000063
2.0	0.0057	0.000025
3.0	0.0060	0.000057

An inspection of Table 6, or the figures which appear in the references, reveals that the attenuation due to oxygen absorption and the attenuation due to water vapor absorption both increase with increases in frequency over the entire frequency range of interest here. Although the amounts of the increases will be different for other altitudes and temperatures, the trend will remain the same. By calculating values of  $\lambda_{H_2O}$

from Tables 6 and 7 one finds that the attenuation due to water vapor will be almost insignificant in comparison to the  $O_2$  attenuation at the low end of the frequency range, even at high absolute humidities, but at the upper end of the frequency range the water vapor attenuation could be a substantial fraction of the  $O_2$  attenuation for high absolute humidities. Since the one-way attenuation due to both oxygen and water vapor is the

TABLE 7. Absolute Humidity in Saturated Air at Sea Level (1013 mb)

(Adapted from the Encyclopedia of Atmospheric Sciences and Astrogeology, edited by R.W. Fairbridge. Copyright © 1967 by Reinhold Publishing Corp. All rights reserved.)

T (°F)	$\rho_v$ (g/m <sup>3</sup> )	T	$\rho_v$
30	4.44	65	15.7
35	5.43	70	18.5
40	6.55	75	21.6
45	7.86	80	25.3
50	9.40	85	29.5
55	11.2	90	34.2
60	13.3	95	39.6

sum of  $A_{O_2}$  and  $A_{H_2O}$ , one would incur little error in calculating attenuation by neglecting  $A_{H_2O}$  at the lower frequencies, but at the high frequencies for high absolute humidities the error could be on the order of tens of percent.

In order to obtain the total one-way attenuation from an elevated source to the ground for gaseous absorption, one determines  $A_{O_2}$  and  $A_{H_2O}$  as functions of altitude and then integrates their sum along the path of propagation. For elevation angles between  $6^\circ$  and  $90^\circ$  the total one-way attenuation in dB due to gaseous attenuation,  $A_c$ , will obey a law of the form

$$A_c = a_0 \csc^2 \theta \quad (22)$$

where  $a_0$  depends on frequency and humidity; for elevation angles between  $0^\circ$  and  $6^\circ$  one must employ a ray trace method for which no simple result appears to exist [7].

By employing interpolation with the data in [7], one finds that for a ground temperature of  $68^\circ\text{F}$  ( $20^\circ\text{C}$ ) and for a relative humidity of 42% the value of  $a_0$  for Eq. (22) at 3 GHz is 0.036. To obtain an approximate

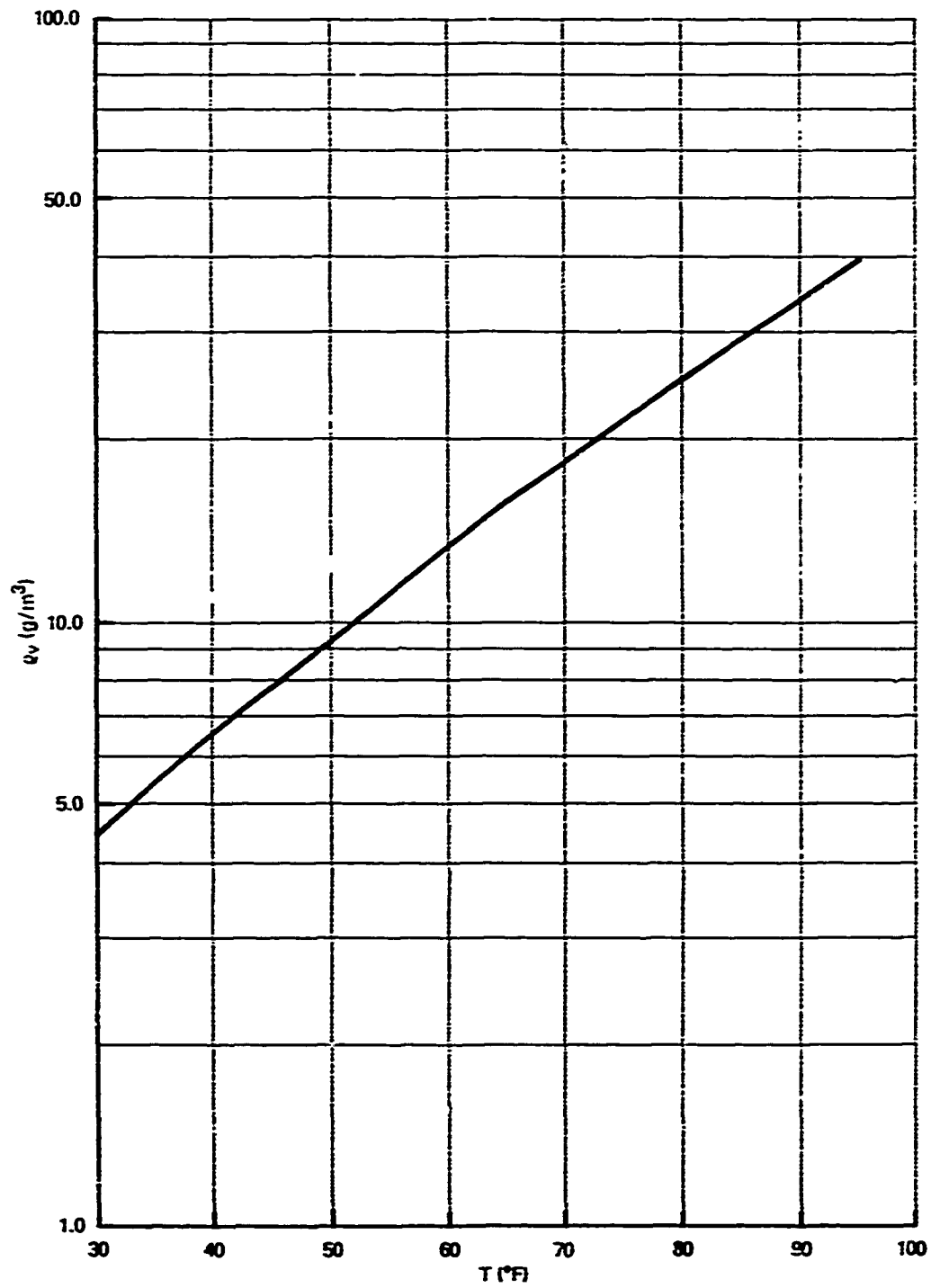


Fig. 7 - Absolute humidity in saturated air at sea level.

value of  $a_0$  at other frequencies one can employ a graph given in [3] (p. 24-20), which gives the attenuation vs. frequency for a low-initial-elevation angle, 300 mile path, for two geographical areas at two times of the year. On the assumption that  $a_0$  should scale as the attenuation values taken from this figure in [3], the curve for Bismarck, N.D. in February was employed to scale the 0.036 value of  $a_0$  at 3 GHz; the results can be seen in Table 8. The Bismarck curve was employed to get the scale factors because the absolute humidity (as opposed to the relative humidity) would be expected to be relatively low in winter, and the 0.036 value of  $a_0$  at 3 GHz was obtained for a value of absolute humidity ( $7.5 \text{ g/m}^3$  at  $68^\circ\text{F}$ , 42% relative humidity) which is too low to have a significant effect on the attenuation. At much higher humidities (say  $20 \text{ g/m}^3$  or more at sea level) the values of  $a_0$  might underestimate the loss by tens of percent at the high frequencies. However, since attenuation at the low end of the frequency range is fairly insensitive to humidity, the values of  $a_0$  for these frequencies should not vary significantly over the observed range of terrestrial absolute humidities. As a final note on the  $a_0$  scaling, the value given in Table 8 for 2 GHz is about 5% less than the calculated value in [7].

TABLE 8. Attenuation Scale Factor and Attenuation Coefficient  $a_0$  (the Attenuation in dB at  $90^\circ$  Elevation) for Gaseous Absorption for Low Humidity

$f$ GHz	Scale Factor	$a_0$
.2	0.15	0.0053
.3	0.25	0.0091
.4	0.35	0.012
.5	0.43	0.016
.6	0.53	0.019
.8	0.59	0.021
1.0	0.68	0.024
2.0	0.88	0.032
3.0	1.0	0.036

### 2.3.2 Antenna Temperature

Oxygen and water vapor radiate r.f. energy which contributes to the

noise temperature of an antenna having a beam that intersects the atmosphere. The noise temperature contributions of these two atmospheric components depend directly on the respective attenuation constants at the frequency of interest ([3], p. 39-5; [9]; [10]). In general, oxygen will contribute more strongly to the noise temperature than will water vapor in the frequency range of interest here; this is particularly true at the low end of the frequency range.

Fig. 8, a composite of figures from [9] and [11], shows the noise temperature due to oxygen and water vapor of a ground-based, narrow beam antenna for several elevation angles; the temperature looking towards the ground from space would be the same provided that the beam was sufficiently narrow. The absolute humidity for which the curves in the figure were calculated was assumed to decrease linearly from  $10 \text{ g/m}^3$  at sea level to zero at an altitude of 5 km.

The maximum and minimum galactic noise components would be important for a space-based, ground-looking system if the surface under observation had a high reflection coefficient and mirrored the sky, as the sea surface does.

### 3. THE IONOSPHERE

The ionosphere is the partially ionized region of the atmosphere that begins at approximately 50 km altitude and is generally defined as ending at about 1000 km altitude. The free electrons in this region change the permittivity from its free space value; the interaction between the earth's magnetic field and the free electrons produces an anisotropy in the permittivity of the region [1]. It is these changes in the permittivity which produce the electromagnetic wave propagation phenomena characteristic of the ionosphere.

The electron density in the ionosphere varies diurnally, geographically, seasonally, with sunspot number and with other solar phenomena. The total electron content, i.e., the electron number density integrated vertically from the bottom to top surface of the ionosphere, can vary by two orders of magnitude depending on the time and location it is measured; predictions of these variations are made by the Air Weather Service of the U.S. Air Force [14]. Because the large temporal and geographical variations in the electron density will produce correspondingly large changes in the magnitude of the observed propagation effects, in order to allow for a conservative analysis the effects will generally be discussed for typical daytime conditions when the ionization has peaked. It should be born in mind that the ionization can increase by a factor of 10 above the typical or average level, however.

The discussion of the ionospheric effects will be restricted to cases in which the observer is located above ionosphere, i.e., at an altitude of at least 1000 km. Space-based radar systems are expected to operate at least this high in order to obtain extensive ground coverage, and hence the dependence of the propagation phenomena on the location of the source within the ionosphere would not be needed. Furthermore, the restriction does allow a considerable simplification to be made in the discussion.

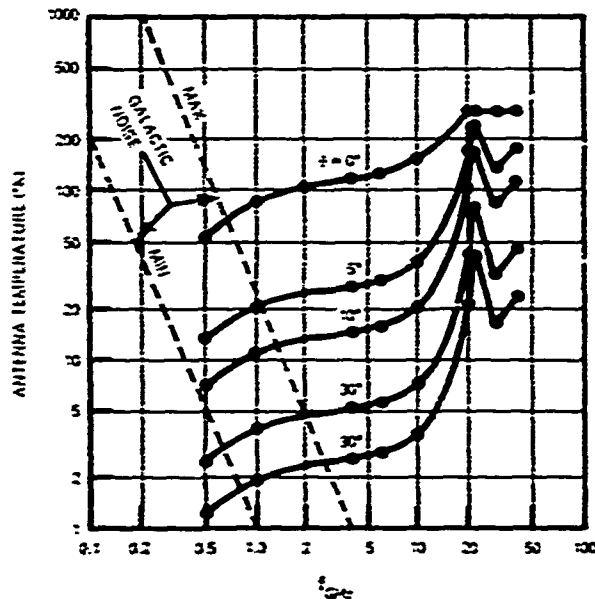


Fig. 3 - Antenna noise temperature due to oxygen and water vapor for several elevation angles for a ground-based antenna.

(Adapted from D.C. Hogg, J. of Applied Physics, 30(9), pp. 1417-1419 (1959), Copyright © 1959 Am. Inst. of Physics, and from J.R. Pierce and R. Kompfner, Transoceanic Communication by Means of Satellites, Proc. IRE, 47, pp. 372-380 (1959), Copyright © 1959 IRE (now IEEE); used by permission.)

### 3.1 Refraction Errors

The calculation of the refraction error introduced by the ionosphere has been examined by numerous investigators (e.g. [2], [15], [16]). Many existing results are for the refraction errors for ground observations of elevated sources, in which cases some manipulation is required in order to get the refraction errors for elevated observers looking at a ground targets.

Fig. 9, obtained from [2], shows the refraction error for a ground observer receiving a 200 MHz signal from a source located in the ionosphere for three different elevation angles. The curves in the figure were derived by using a layered model of the ionosphere for daytime ionization levels. If one lets  $\tilde{\Delta\alpha}_G$  represent the refraction error (in radians) at the ground when observing at source located at an altitude of 1000 km, one finds that the equation

$$\tilde{\Delta\alpha}_G(\theta) = 0.00033c\theta \quad (23)$$

fits the data in the figure to an accuracy of better than 15%. However, since ionospheric refraction remains relatively constant between 0° and 5° elevation [13] or possibly may exhibit a slight increase as  $\theta$  increases in this range [16], Eq. (23) should not be employed at less than 10° elevation. Letting  $\tilde{\Delta\alpha}_O$  represent the ionospheric refraction error for an observer at 1000 km altitude looking at a ground target, it is shown in Appendix C that the following relationship can be obtained:

$$\tilde{\Delta\alpha}_O(\theta) = \frac{(1-n_1)\cos\theta - \tilde{\Delta\alpha}_G(\theta)\sin\theta}{\left[\left(1 + \frac{h_1}{r_0}\right)^2 - \cos^2\theta\right]^{1/2}} \quad (24)$$

Here  $h_1$  is the height of the observer, 1000 km,  $r_0$  is the radius of the earth, and  $n_1$  is the real part of the ionospheric refractive index at altitude  $h_1$ . At frequencies of interest here one has (neglecting losses and magnetic bias) [15]

$$n_1 \approx 1 - \frac{1}{2} \frac{\omega_p^2(h_1)}{\omega^2} \quad (25)$$

where  $\omega$  is the angular frequency of the propagating wave, and where  $\omega_p$  is the (angular) plasma frequency defined by

$$\omega_p^2(h) \equiv \frac{n_e(h)e^2}{m_e\epsilon_0} \quad (26)$$

The quantities  $n_e(h)$ ,  $e$ , and  $m_e$  are, respectively, the number density of the electrons at altitude  $h$ , the charge of an electron, and the mass of an electron.

The results in Appendix A can be used to obtain the refraction error at altitude  $h > h_1$  if there is negligible bending of the wave between altitudes  $h_1$  and  $h$ . Letting  $\tilde{\Delta\alpha}(\theta, h)$  represent the refraction error at altitude  $h$  where  $\theta$  is still the elevation angle of the observer measured from ground level, one has

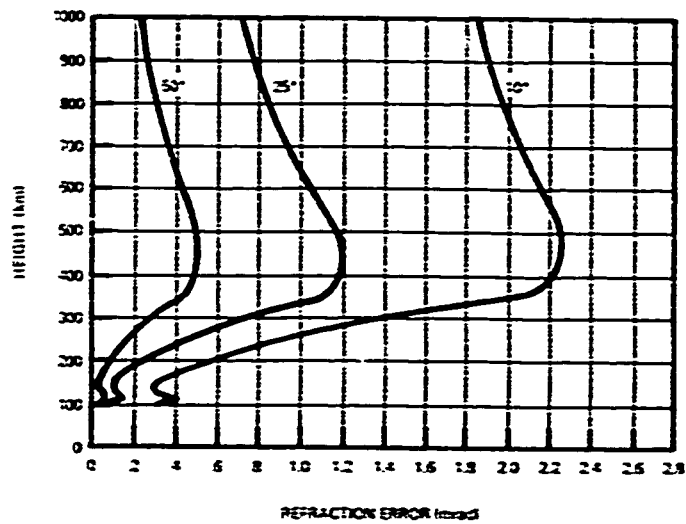


Fig. 9 - Daytime ionospheric refraction error for a ground observer of a 200 MHz elevated source for three elevation angles.

(From G.H. Millman, Atmospheric Effects on VHF and UHF Propagation, Proc. IRE, 46, pp. 1492-1501 (1958), Copyright © 1958 IRE (now IEEE), used by permission.)

$$\tilde{\Delta\alpha}(\vartheta, h) = \tilde{\Delta\alpha}_0(\vartheta) \frac{[\sin^2\vartheta + 2(\frac{h_1}{r_0}) + (\frac{h_1}{r_0})^2]^{1/2} - \sin\vartheta}{[\sin^2\vartheta + 2(\frac{h}{r_0}) + (\frac{h}{r_0})^2]^{1/2} - \sin\vartheta} =$$

$$\frac{(1-n_1-0.00033)\cos\vartheta}{[(1+\frac{h_1}{r_0})^2 - \cos^2\vartheta]^{1/2}} \frac{[\sin^2\vartheta + 2(\frac{h_1}{r_0}) + (\frac{h_1}{r_0})^2]^{1/2} - \sin\vartheta}{[\sin^2\vartheta + 2(\frac{h}{r_0}) + (\frac{h}{r_0})^2]^{1/2} - \sin\vartheta}$$

where Eq. (23) for  $\tilde{\Delta\alpha}_0$  has been employed. In terms of the straight line distance  $D(\vartheta, h)$  between the target and the observer, one can write Eq. (27) as

$$\tilde{\Delta\alpha}(\vartheta, h) = \frac{(1-n_1-0.00033)\cos\vartheta}{[(1+\frac{h_1}{r_0})^2 - \cos^2\vartheta]^{1/2}} \frac{D(\vartheta, h_1)}{D(\vartheta, h)}. \quad (28)$$

Eqs. (27) and (28) are not valid for  $\vartheta < 10^\circ$  since Eq. (23), employed in obtaining these two equations, is not accurate below  $10^\circ$  elevation.

In order to obtain concrete results from Eq. (28) one must know  $n_1$ , or equivalently  $n_e(h)$  in view of Eq. (26). Employing the Chapman formula for the electron density given in [2] with a scale height  $H$  of 100 km and values of  $1.25 \times 10^{12}/m^3$  and 300 km for the maximum electron density  $N_m$  and the height  $h_m$  of the maximum density, respectively, one obtains  $n_e(h_1) = 6.2 \times 10^{10}/m^3$ . Employing this value of  $n_e$  in Eq. (26), and using the resulting value of  $\alpha_0$  in Eq. (25), one finds that  $1 - n_1 = 6.3 \times 10^{-5}$  at 200 MHz. Using this value in Eq. (28), one obtains for 200 MHz the result

$$\tilde{\Delta\alpha}(\vartheta, h) = - \frac{0.00027\cos\vartheta}{[(1+\frac{h_1}{r_0})^2 - \cos^2\vartheta]^{1/2}} \frac{D(\vartheta, h_1)}{D(\vartheta, h)}. \quad (29)$$

At  $\vartheta = 10^\circ$ , the minimum elevation angle for which Eq. (29) can be employed, one finds that the refraction error is approximately equal to -0.44 milliradians at  $h = h_1$ , where the negative sign indicates that the propagating wave will approach the elevated observer from below the direct path to the target, rather than from above the path as shown for  $\Delta\alpha_0$  in Fig. 1.

It should be noted that the value of  $n_e(h_1)$  calculated from the data in [2] and employed in obtaining Eq. (29) is a factor of 2 less than the measured peak value of  $n_e$  given in [17], from which Fig. 10 has been taken. (The  $N_m$  in this figure is the total number of electrons in a vertical

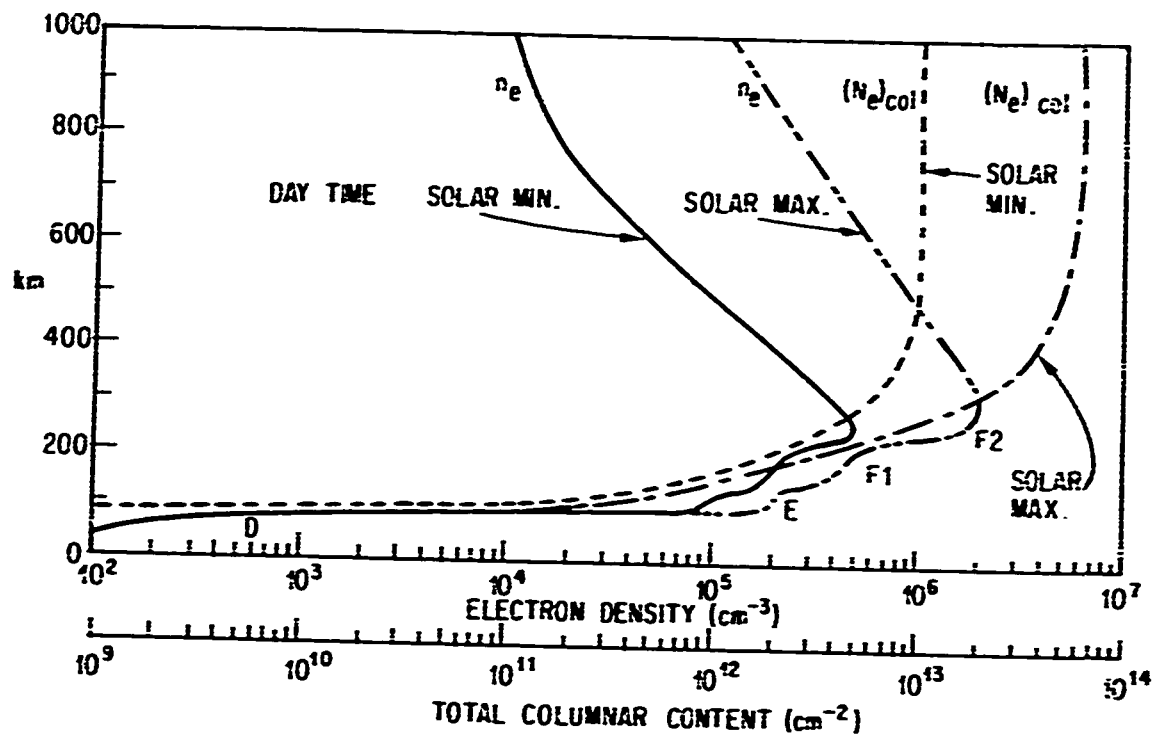


Fig. 10 - Daytime ionospheric electron density and columnar content.

(From M.A. Kasha, The Ionosphere and its Interaction with Satellites, Chapter 2, Gordon and Breach, Science Publishers, Inc., Copyright © 1969, used by permission.)

column of unit cross-sectional area.) However, since the bending of the propagation path is still relatively slight at altitudes on the order of  $h_1$ , the inaccuracies in the electron densities at these altitudes are not expected to cause more than a 20%-25% change in the calculated value of the refraction error, which amounts to no more than 0.1 milliradians at  $\theta=10^\circ$ . Since the purpose here is to determine the magnitude of the propagation effects, this uncertainty in the refraction error is acceptable. A more precise design study might require a more exacting analysis, however.

One can show from Eq. (29) (or Eq. 27) that the refraction error magnitude will decrease with increases in the elevation angle for elevation angles greater than  $10^\circ$ . The equation cannot be employed at angles below  $10^\circ$ , as stated earlier. Eq. (29) also reveals that the angular refraction error magnitude for a given  $\theta$  will decrease as observer altitude increases (since  $D(\theta, h) > D(\theta, h_1)$  for  $h > h_1$ ). However, it was noted earlier that the equation is valid only if there is negligible bending of the propagation path between altitudes  $h_1$  and  $h$ . Since the electron density, and consequently the refractive index, exhibits a gradient even at quite high altitudes (see Fig. 11 taken from [17]), there will be a bit of additional bending of the propagation path and the refraction error will differ slightly from the value given by Eq. (29).

At night the refraction errors will be less than those seen during the day. In [2] the refraction errors seen by a ground observer tracking an elevated target were found to be a factor of 2.7 less at night in comparison to the daytime errors; the refraction errors seen by an elevated observer tracking a ground target should show a similar decrease.

The numerical results given so far are for a 200 MHz wave. The ionospheric refraction error in the frequency range of interest here is proportional to the inverse square of the frequency [13]. The error is probably of no more than marginal importance at 200 MHz, and would almost certainly be inconsequential at higher frequencies.

The ionospheric refraction errors were calculated without taking into account tropospheric refraction. Although in an exact analysis the two types of refraction errors must be dealt with simultaneously and cannot be separately calculated and added, at the very small refraction errors seen at frequencies of interest here separate calculation and subsequent addition of the individual errors is a very good approximation [16].

### 3.2 The Iris Effect

The real part of the refractive index of a lossless or slightly lossy plasma will be less than unity, and as a consequence a wave incident on the ionosphere will undergo total internal reflection ([18], p. 145) if the angle of incidence (angle between the direction of propagation and the ionospheric surface normal) is greater than a critical value  $\phi_c$ . As a consequence, waves whose directions of propagation lie outside of a particular cone whose apex is the elevated observation point and whose axis is normal to the ionosphere will not penetrate the ionosphere; the effect is known as the iris effect [13] and is illustrated in Fig. 12.

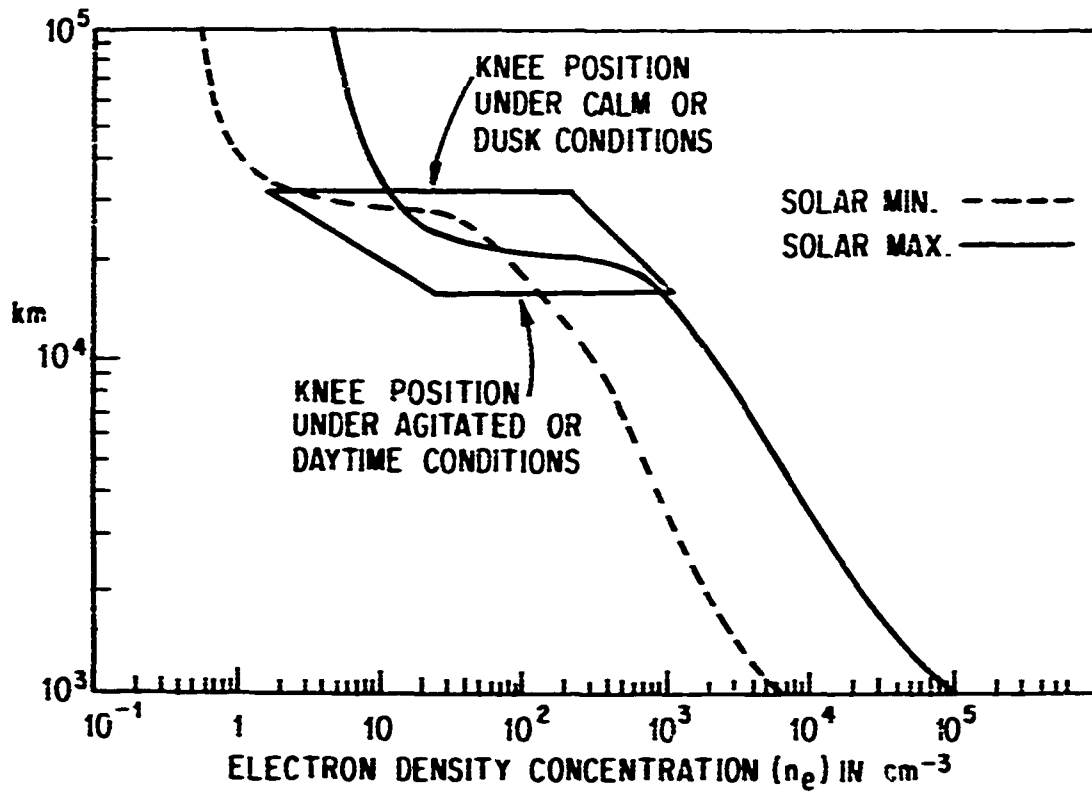


Fig. 11 - Electron densities at extreme altitudes

(From M.A. Kasha, The Ionosphere and its Interaction with Satellites, Chapter 2, Gordon and Breach, Science Publishers, Inc., Copyright © 1969, used by permission.)

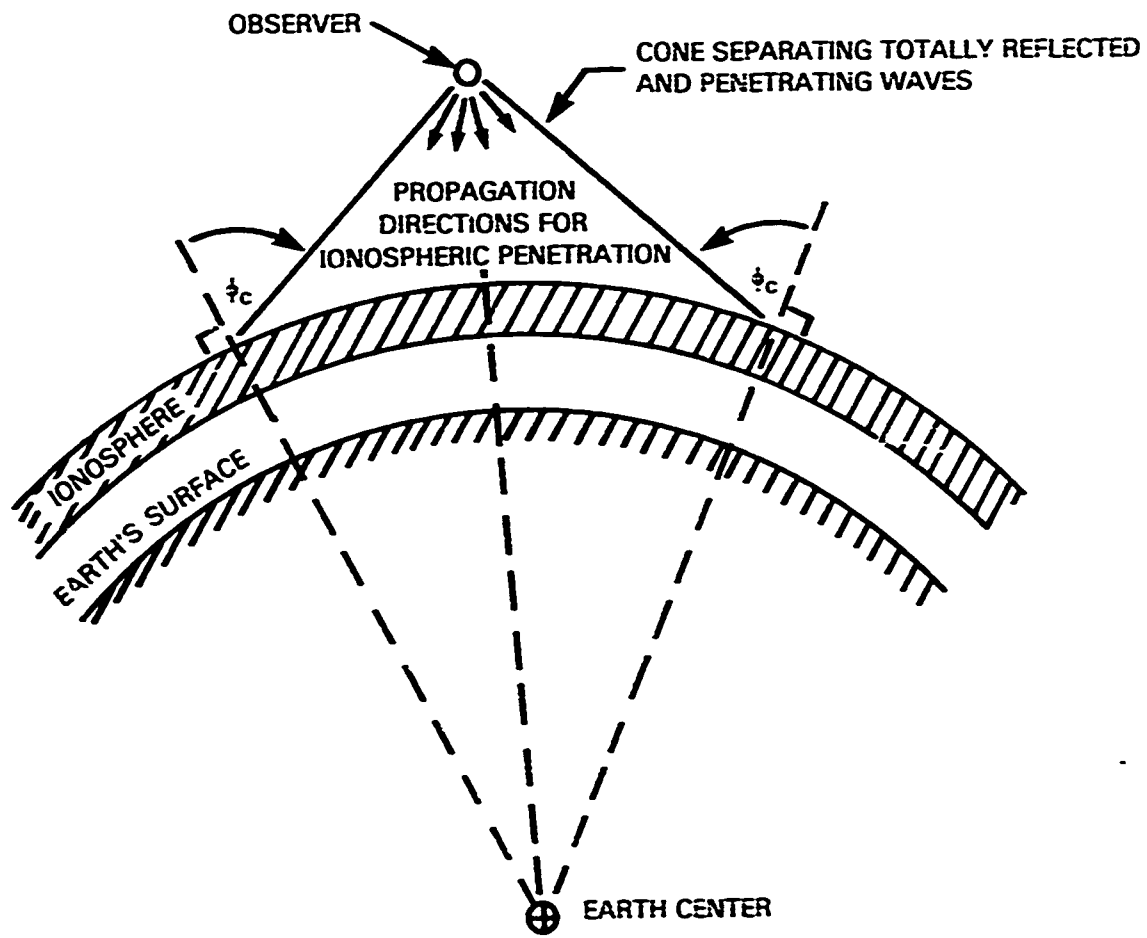


Fig. 12 - The iris effect.

Critical angle  $\phi_c$  is equal to  $\sin^{-1}(n_m)$  [13] where  $n_m$  is the minimum value of the refractive index in the ionosphere, i.e., the refractive index at the height of maximum electron density. The maximum electron density appears in the F layer of the ionosphere at an altitude of approximately 300 km. Employing for  $(n_e)_{\max}$  the value of  $2 \times 10^{12}/m^3$  taken from Fig. 10, and utilizing the expression for the refractive index given by Eq. (25), one can determine the critical angle for any frequency of propagation. Table 9 lists the values of  $\phi_c$  for a number of frequencies.

The iris effect could affect an elevated observer surveying the earth's surface by blocking the waves directed at certain portions of the surface, rendering these portions unobservable. However, one can easily show that a ray tangent to the earth's surface will intersect an ionospheric layer at the 300 km altitude at an angle of about  $72.6^\circ$  with respect to the normal of the layer. Since this value is considerably less than the smallest  $\phi_c$  value in Table 9, there will be no blockage here of rays by the iris effect to any portion of the earth's surface. The iris effect thus has no impact on an earth surveillance system operating at current frequencies of interest.

TABLE 9. Critical Angle of Incidence for the Iris Effect

$f_{\text{GHz}}$	$\phi_c$
0.2	$86.4^\circ$
0.5	$88.6^\circ$
1.0	$89.3^\circ$
2.0	$89.7^\circ$
3.0	$89.8^\circ$

### 3.3 Doppler Errors

The bending of the propagation path by the ionosphere will cause the doppler frequency induced by target motion to differ from what would be obtained if the propagation path were the straight line between the target and source. The expression for the relative doppler error is nearly identical to that given by Eq. (6) for the error introduced by tropospheric refraction, the difference being the replacement  $\Delta\alpha_G(\theta)$  by  $\Delta\tilde{\alpha}_C(\theta)$ . Thus the relative doppler error caused by ionospheric refraction is

$$\frac{\Delta f_d}{f_d} = \tilde{\Delta \alpha_G}(\theta) \sin \psi \quad . \quad (30)$$

The expression for  $\tilde{\Delta \alpha_G}(\theta)$  for 200 MHz, 1000 km altitude, and daytime conditions was given by Eq. (23). Employing this in Eq. (30), one obtains

$$\frac{\Delta f_d}{f_d} = 0.00033 \text{ctn} \theta \sin \psi \quad . \quad (31)$$

Because of the limitations on Eq. (23), the above equation is not valid for  $\theta < 10^\circ$ . At altitudes above 1000 km  $\tilde{\Delta \alpha_G}$  will differ slightly from the value given by Eq. (23) due to the additional ray bending introduced by the longer propagation path in the plasma, as noted at the end of the section on ionospheric refraction. As also mentioned in the section on refraction, the expression for  $\tilde{\Delta \alpha_G}$  may be slightly inaccurate due to inaccuracies in the electron density model employed in [2] at the higher elevations. These inaccuracies in the value of  $\tilde{\Delta \alpha_G}$  will lead to inaccuracies of a similar magnitude in the value of the relative doppler error given by Eq. (31).

At night  $\tilde{\Delta \alpha_G}$  is a factor of 2.7 less than its daytime value, as mentioned earlier. The relative doppler error at night will then be decreased by the same factor.

The previously mentioned proportionality between the refraction error and the inverse square of the frequency implies that the relative doppler error will also decrease as the inverse square of the frequency. Thus the error at 400 MHz would be one-quarter of the value given by Eq. (31).

The total relative doppler error in a system is proportional to the total refraction error introduced by ionospheric and tropospheric effects. As mentioned in the section on ionospheric refraction, the refraction error for situations of interest can be closely approximated by adding the individual refraction errors due to the ionosphere and the troposphere. The total doppler error can therefore be closely approximated by adding the individual ionospheric and tropospheric doppler errors.

### 3.4 Range Errors

The ionosphere is a dispersive medium which will introduce an additional time delay in a propagating signal over what would be expected for a free space propagation path. This additional time delay is calculated from the group velocity of electromagnetic waves propagating in the medium [2], [13].

Plots of range error versus altitude for different frequencies and elevation angles can be found in [2]. Employing the plot corresponding to a decaying electron density above the F-layer distribution and a 200 MHz frequency, one finds that the day range error  $\Delta D(\theta)$  caused by the ionosphere is given quite accurately at 1000 km altitude by

$$\tilde{\Delta D}(\theta) = 310 \text{csc} \theta', \quad (32)$$

where

$$\theta' = \cos^{-1} \left( \frac{\cos \theta}{1 + h_2/r_0} \right), \quad (33)$$

and where  $h_2 = 250$  km;  $\Delta D$  is in units of meters here. Parameter  $\theta'$  is the angle a ray emanating from the ground at elevation angle  $\theta$  would make with the tangent plane at the point the ray would intersect an ionospheric layer at altitude  $h_2$ . Eq. (32) is accurate for  $\theta > 10^\circ$ , and probably gives good results down to  $\theta = 0^\circ$ .

The plot from which Eq. (32) was derived shows that the range errors are nearly independent of altitude at the 700 km altitude and above, so that Eq. (32) can be used for altitudes in excess of 1000 km.

The range error introduced by the ionosphere is proportional to the inverse square of the frequency for the frequency range of interest here, just as in the case of the refraction error. At 200 MHz, Eq. (32) gives a value of 294m; at 400 MHz the error would be one-fourth this value.

From the data in [2] one would expect the night-time range errors to be less than the daytime values by a factor of about 3.5, close to the 2.7 factor found for the refraction errors.

### 3.5 Attenuation:

Below a certain critical frequency the ionosphere is essentially opaque to electromagnetic waves. This frequency is given by Eq. (26) at the altitude  $h$  of maximum electron density. Employing for the maximum value of  $n_e$  the  $2 \times 10^{12}/\text{m}^3$  figure used in the section on the iris effect, one obtains 12.7 MHz for the critical frequency, a typical value for this parameter and well below the minimum frequency of interest here.

Waves with frequencies above the critical frequency can propagate in the ionosphere, but they will suffer attenuation due to collisions between the plasma electrons and the other particle species comprising the ionosphere. This attenuation is frequency dependent, being inversely proportional to the square of the frequency in the range of frequencies being considered here.

Fig. 13, based on the data in [2], shows the one-way daytime ionospheric absorption loss. Although the data in [2] was for a 1000 km altitude, the facts that the columnar electron content is increasing very slowly at this altitude and above (see Fig. 10) and that the electron collision frequency is decreasing with altitude ([19], Table 7.8), together with knowledge that the attenuation is proportional to the integral over the propagation path of the product of electron density and electron collision frequency, imply that attenuation will increase very slowly above the 1000 km level. The values in the figure can therefore apply to observers at several thousand kilometers altitude.

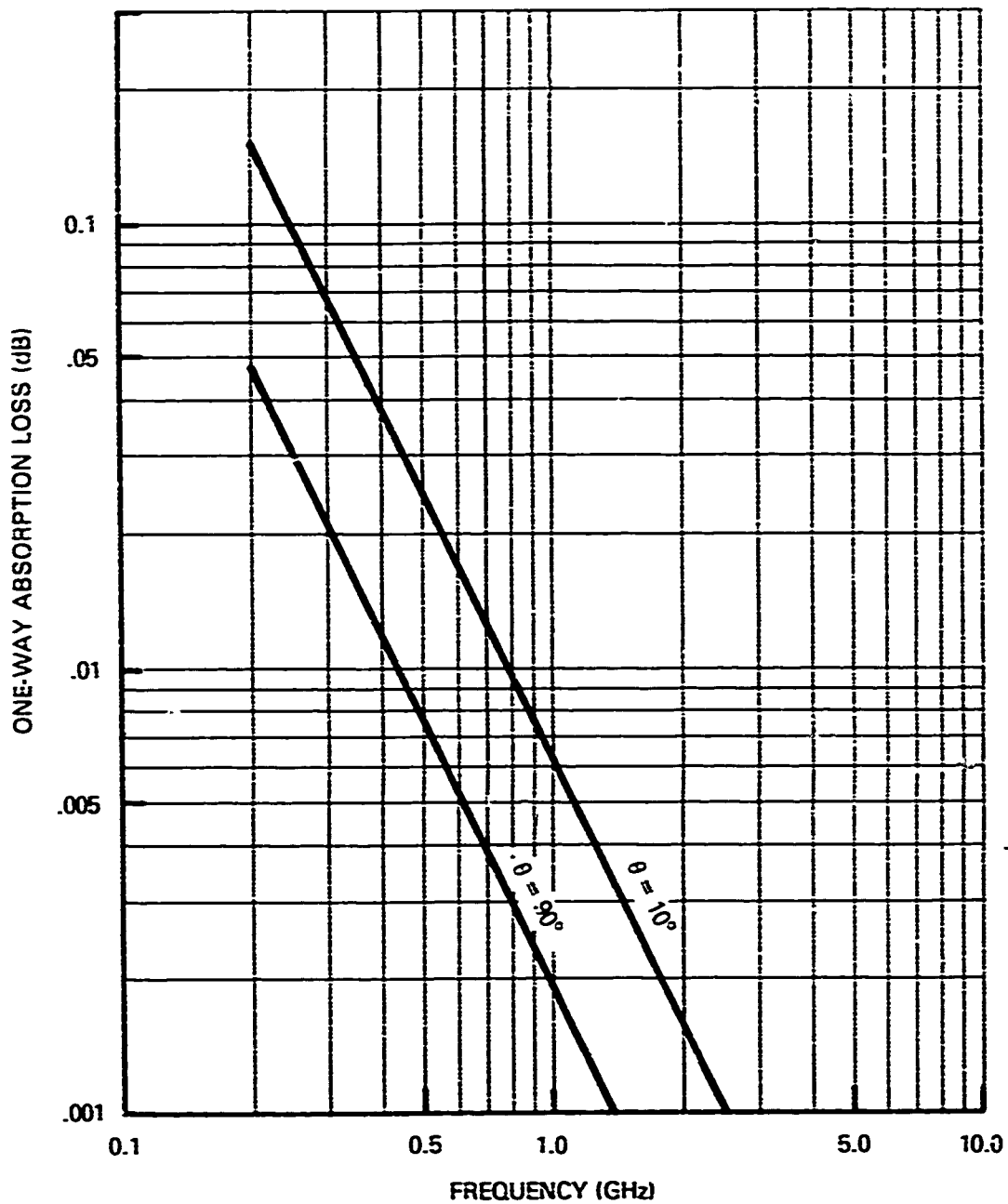


Fig. 13 - One-way ionospheric loss in the daytime.

It can be seen from Fig. 13 that the two-way ionospheric absorption loss will be less than 0.4 dB at the minimum frequency of interest here, 200 MHz. The data in [2] and [13] indicate that at night the loss will decrease by a factor of 10 to 20.

Before concluding this section on absorption loss, two types of ionospheric phenomena which cause unusually high absorption will be mentioned. The first of these are the auroral absorption events which occur in conjunction with luminous aurora, mainly at the higher geomagnetic latitudes [13]. These events, which can occur daily in the auroral zone during the equinoctial months and which persist from several minutes to several hours, can cause increases in the absorption loss of from 6 to 20 times the typical daytime dB value. The second type of ionospheric phenomena is the polar-cap absorption event, which can increase the absorption loss by a factor of 20 to 60 times its typical daytime value, according to data in [13]. The absorption increase extends from the polar caps down to the equatorial limits of the auroral zones. The polar cap event is caused by an influx of protons produced by a solar flare, and is most frequently seen during the peak of the sunspot cycle. The event can persist for several days.

### 3.6 Polarization Effects

The presence of the earth's magnetic field in the ionospheric plasma results in the plasma exhibiting an anisotropy in its permittivity [12], [19]. Two modes of electromagnetic wave propagation are possible in this anisotropic medium, the "ordinary" waves and the "extraordinary" waves, and in general a plane wave propagating in this medium will be a combination of these two modes. Since the two modes have different propagation constants associated with them, a wave propagating through the medium can exhibit a rotation of its polarization plane and/or a change in the type of polarization (e.g., from linear to elliptical).

For frequencies of interest here, the type of polarization will not change during propagation through the ionosphere except when the direction of propagation is almost exactly transverse to the geomagnetic field [13]. The transition angle  $\theta_c$  between the direction of propagation and the geomagnetic field at which the type of polarization starts to change is listed in Table 10 for several frequencies of interest.

Although the type of polarizations will not change if the angle between the direction of propagation and the geomagnetic field is less than the transition angle, the plane of polarization can rotate. This rotation can cause a loss of power at the reception antenna. For example, for a linearly polarized antenna the power loss would vary as  $\cos^2\phi$  where  $\phi$  is the angle between the plane of polarization of the wave and the plane of polarization of the antenna.

TABLE 10. Transition Angle at which Type of Polarization Begins to Change

$f$ GHz	$\theta_c$
0.2	89.76°
0.5	89.90°
1.0	89.95°
3.0	89.98°

The amount of polarization rotation depends on the angle between the direction of propagation and the geomagnetic field; the rotation is a maximum when the direction of propagation and the direction of the geomagnetic field coincide, i.e., when the propagation is strictly "longitudinal" [13]. Thus the amount by which the plane of polarization rotates will depend not only on the elevation angle of the observer but also on his azimuth.

In [2] a plot is given of the phase change between the two propagation modes for longitudinal propagation of a 200 MHz wave for a two-way path. The polarization rotation is equal to one-half of the phase change between the two components [13], so the one-way polarization rotation is equal to one-fourth of the two-way phase change. Fig. 14 shows the one-way polarization rotation calculated from the phase change plot in [2]. The loss scales in the figure show the one-way loss and the two-way loss (i.e., for twice the one-way rotation angle) for linearly polarized antennas due to rotation of the plane of polarization. Although the data in [2] was given for an altitude of 1000 km, the low electron densities above this altitude, and consequently their minimal effect on rotation, allow one to use the data at much higher altitudes.

It was noted earlier that polarization rotation is a maximum for longitudinal propagation, and will be less when the direction of propagation is not aligned with the geomagnetic field. Thus the plots in Fig. 14 represent upper bounds on the polarization rotation over all possible azimuths and latitudes.

It is interesting to note that since both the range error and the longitudinal polarization rotation are proportional to the integral of the electron density along the path of propagation they should both exhibit the same dependence on elevation angle. Hence the rotation should be proportional to  $\csc \theta'$  where  $\theta'$  is defined by (33). If one employs the  $\theta=90^\circ$  rotation values given in Fig. 14 and computes the rotation at  $\theta=10^\circ$  using this assumed angular dependence, the values obtained differ from those in the figure by 11%.

At night the rotation is a factor 3.5 less than its daytime value [2]. This is the same factor that was observed in the case of the range errors.

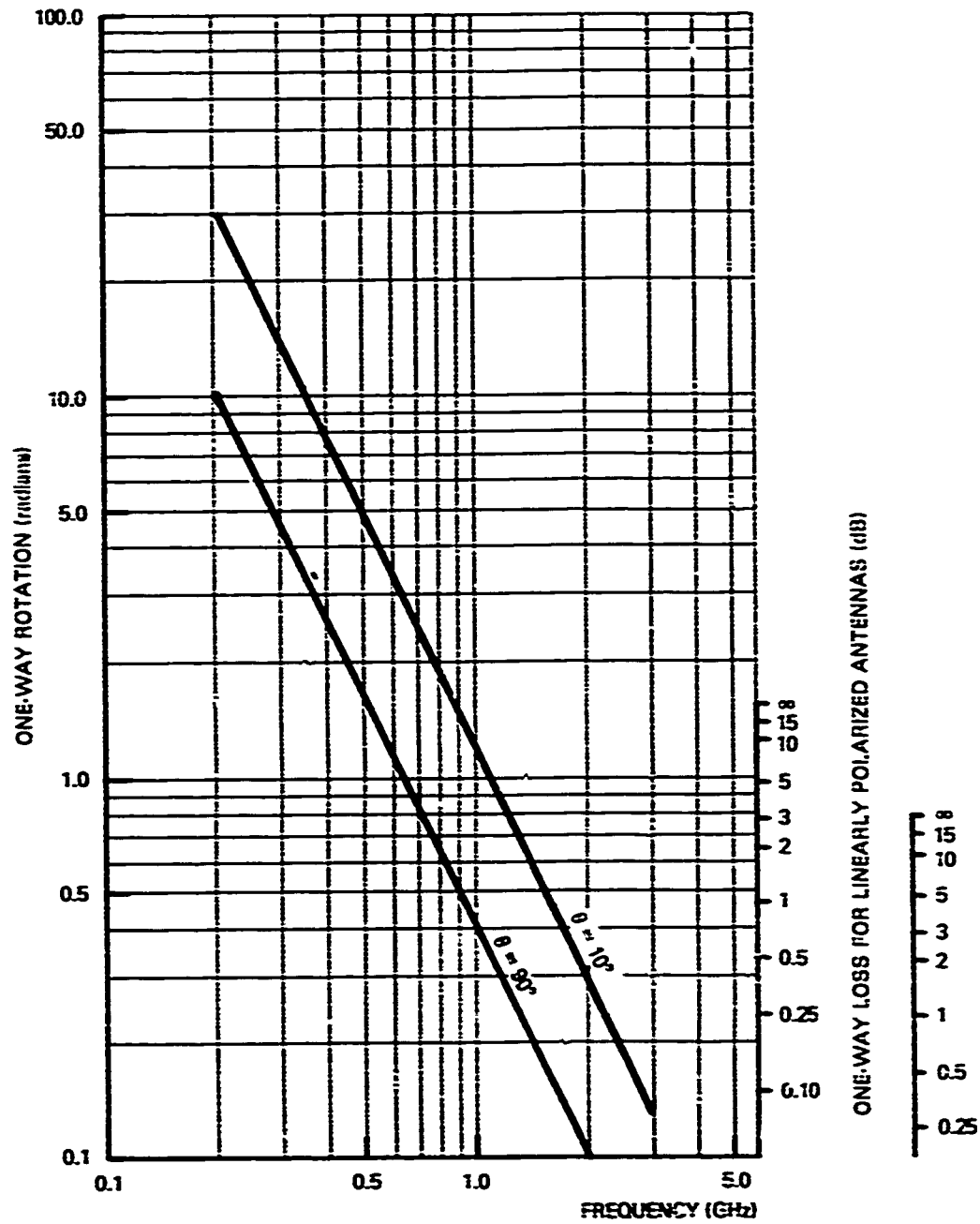


Fig. 14 - One-way polarization rotation for longitudinal propagation in the ionosphere in daytime.

### 3.7 Scintillation

Another ionospheric propagation phenomenon which may affect radar system performance is scintillation, the temporal fluctuation in amplitude and phase of waves which have traversed the ionosphere. The phenomenon is attributed to diffractive and focusing/defocusing effects of elongated irregularities or inhomogeneities in the electron density, primarily in the F layer [20], [21]. The irregularities typically have dimensions of 1 km in directions transverse to the geomagnetic field and lengths of 4 km to 100 km along the field [21]; they exhibit drift velocities of 20-300 m/s [21].

Early data on the scintillation of high-frequency radio waves came from radio astronomical observations, as noted in [22], but most of the recent data has come from terrestrial observations of satellite signals [23], [24]. Many questions remain to be answered about the phenomenon and consequently it is still the subject of much current research, as a study of the papers in [25] will reveal.

The geographical areas where scintillation is of a sufficient magnitude to cause problems with radiowave systems are shown in Fig. 15, taken from [26]. The density of the shading in the figure indicates the depth of the fading associated with scintillation, the darkest shading indicating the deepest fading. The latitudes shown in the figure are the geomagnetic (also called invariant) latitudes, which are based on geomagnetic field lines; the relationship between these latitudes and the geographic latitudes are shown in Fig. 16, taken from [21].

It is seen from Fig. 15 that the regions where scintillation is significant are the polar/auroral regions and the equatorial region in the pre-midnight and early morning hours. The physical processes believed to be the causes of the ionospheric irregularities are different in the equator and polar/auroral regions. In the former the irregularities are attributed to plasma instabilities, while in the latter particle precipitation is believed to be the cause [21]. There are likewise differences in the nature of the scintillation observed in these regions and in the influence of seasonal and other factors on scintillation; data on these subjects will now be presented.

Amplitude scintillation measurements will be presented first. Since the data were taken under a variety of different conditions one cannot generally draw conclusions from comparisons of the various values. Instead, one should use the data to gauge the magnitude of the effects to be expected. Near the equator, peak-to-peak amplitude fluctuations of 29 db have been observed in the 259 MHz signal from the MARISAT I satellite in Natal, Brazil [27], while 27 db fluctuations were observed in a 1541 MHz signal at Ascension Island during a time frame in which fluctuations of 6.8 db and 8 db were recorded at Huancayo, Peru and Natal, respectively [28]. Amplitude fluctuations of 9 db have been observed at 4 GHz in Hong Kong [29]. In the northern areas where scintillation is significant peak-to-peak fluctuations of 30 db have been recorded at Millstone Hill, MA, in the 150 MHz signals received from the U.S. Navy Navigational system satellites [21].

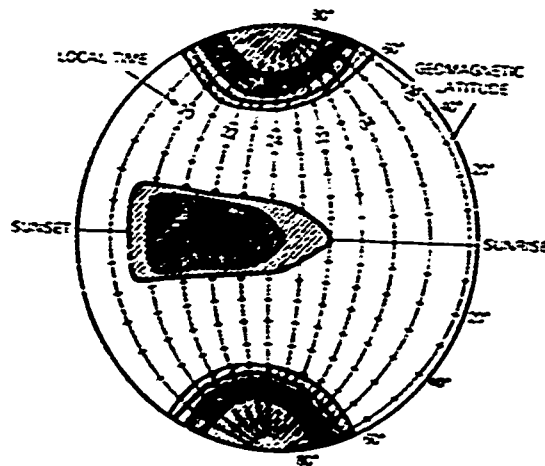


Fig. 15 - Geographical areas characterized by scintillation with deep fading. (From [26] )

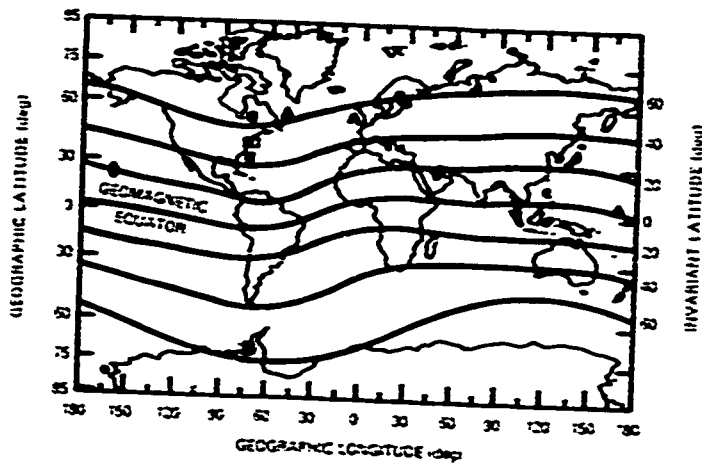


Fig. 16 - Relationship between geographic and invariant (geomagnetic) latitudes.  
 (From R.K. Crane, Ionospheric Scintillation, Proc. IEEE, 65, pp. 180-199, Copyright © 1977 IEEE, used by permission.)

Data on phase scintillation are not nearly as plentiful in the literature as that on amplitude scintillation, possibly because phase measurements are more difficult to make than amplitude measurements. Phase fluctuations of a few radians have been observed at L-band (1575 MHz and 1228 MHz) at Kwajalein, Marshall Islands [29]. Fluctuations of a similar magnitude have also been observed at Poker Flats Rocket Range, just north of Fairbanks, Alaska, in the 1239 MHz signal of the multifrequency beacon of a Navy Navigation Satellite; simultaneously, phase fluctuations which appear to have magnitudes in the tens of radians were observed in the 138 MHz signal of the beacon [30].

Knowledge of the fluctuation frequencies that characterize scintillation is also required for an understanding of the phenomenon. These frequencies vary substantially from the equatorial to the polar/auroral regions. In the polar/auroral regions the period of the peak-to-peak fluctuations is typically 1-3 seconds, while in the equatorial region the period is a factor of 2-10 longer [23]. The spectra of some phase and amplitude scintillation observed at Millstone Hill, MA, can be found in [31]. Amplitude scintillation spectra observed at Huancayo, Peru at 254 MHz and at Narssarssuaq, Greenland, can also be found in [32]. In this last reference, statistics on the amplitude scintillation are employed to produce plots showing data channel reliability for different message lengths and signal threshold levels.

Scintillation exhibits diurnal and seasonal changes, and it is also influenced by geomagnetic and solar conditions. Equatorial scintillation tends to be a maximum about the time of the equinoxes and a minimum about the time of the solstices [21], [23]. Scintillation increases with increasing sunspot number [28], [33], [34]. Scintillation in the polar/auroral region increases during magnetic storms [21] (disturbances of the geomagnetic field frequently, but not invariably, caused by particle influx from solar flares, and typically lasting 3-72 hrs [35]). In the equatorial region magnetic storms cause scintillation to decrease during periods of high sunspot number, but the effect is unclear during periods when the number is low [21], [23].

Scintillation varies with azimuth and elevation angle, the phenomenon becoming more pronounced at azimuths parallel to the local geomagnetic field and at elevation angles approaching 0°. Fig. 17, taken from [21], shows the angular correction factors for  $\sigma_x$ , the variance of the log of the signal amplitude and one of the common measures of amplitude scintillation. The axial ratios in the Figure are the ratios of the longitudinal to transverse dimensions of the ionospheric irregularities producing the scintillations.

A factor of particular interest which affects scintillation is the frequency. The  $S_4$  index, the variance of the intensity fluctuations and another common measure of amplitude scintillation [20], is commonly taken to exhibit an  $f^{-1.5}$  dependence on frequency, although the -1.5 exponent may be somewhat in error for GHz frequencies [21], [33]. The rms phase (or doppler) fluctuations are generally accorded an  $f^{-1}$  frequency dependence.

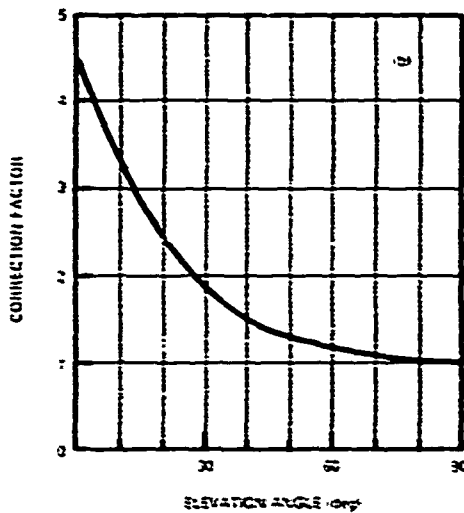
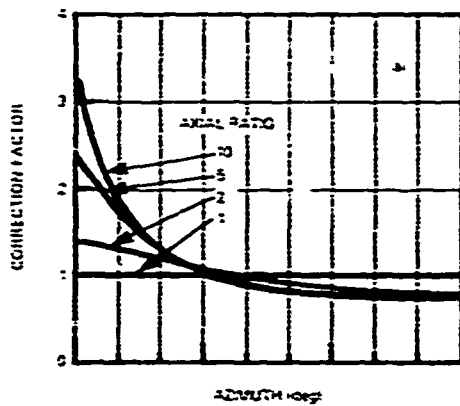


Fig. 17 - Correction factors for  $\sigma_y$  for (a) azimuth relative to geomagnetic field and for (b) elevation angle.

(From R.K. Crane, Ionospheric Scintillation, Proc. IEEE, 65, pp. 180-199, Copyright © 1977 IEEE, used by permission.)

As a final note on scintillation, it has been observed that the phase fluctuations have a Gaussian distribution whereas the intensity fluctuations are well characterized by the Nakagami- $m$  distribution

$$p(x) = \frac{\pi^m x^{m-1}}{\Gamma(m) \bar{x}^m} e^{-\pi x/\bar{x}} \quad (34)$$

where

$$m \equiv S_4^{-2},$$

$S_4$  being the variance of the intensity fluctuations mentioned above; more elaborate distribution functions which exhibit the observed correlation between phase and amplitude scintillation have also been derived [36].

#### 4. CONCLUSIONS

The major trade-off to be made in selecting a frequency in the 0.2-3.0 GHz range for a space-base radar, insofar as propagation and scattering effects are concerned, is the relative insensitivity of the lower frequencies to weather-related phenomena versus the relative immunity of the higher frequencies to ionospheric effects. Clutter due to precipitation appears to be the most significant weather-related phenomenon; a complete assessment of its effect on a system requires a knowledge of the antenna pattern and other system parameters, however. The most important ionospheric effect is the Faraday rotation, although scintillation may also be a problem. At the lower frequencies the use of circular polarization, or some means of adaptively changing the polarization of the antenna upon reception, appears mandatory; moreover, during extremely intense periods of ionization such techniques might be needed even at the higher frequencies.

#### 5. REFERENCES

1. R.W. Fairbridge, Ed., The Encyclopedia of Atmospheric Sciences and Astrogeology, Reinhold Publishing Corp., New York, 1967.
2. G.H. Millman, "Atmospheric Effects on VHF and UHF Propagation", Proc. IRE, 46(8), pp. 1492-1501, 1958.
3. M.I. Skolnik, Ed., Radar Handbook, McGraw-Hill Book Company, New York, 1970.
4. D.E. Kerr, Ed., Propagation of Short Radio Waves, Dover Publications, Inc., New York, 1965.
5. R.L. Olsen, D.V. Rogers, and D.B. Hodge, "The  $\alpha R^0$  Relation in the Calculation of Rain Attenuation", IEEE Trans. Antennas Propagat., AP-26(2), pp. 318-329, 1978.
6. K.L.S. Gurn and T.W.R. East, "The Microwave Properties of Precipitation Particles", Quart. J. Roy. Meteorol. Soc., 80, pp. 522-545, 1954.

7. L.J. Ippolito, "Radio Propagation for Space Communications Systems", Proc.IEEE, 69(6), pp. 697-727, 1981.
8. R.P. Auty and R.H. Cole, "Dielectric Properties of Ice and Solid D<sub>2</sub>O", J. Chem. Phys., 20(8), pp. 1309-1314, 1952.
9. D.C. Hogg, "Effective Antenna Temperatures Due to Oxygen and Water Vapor in the Atmosphere", J. Appl. Phys., 30(9), pp. 1417-1419, 1959.
10. E.K. Smith, "Centimeter and millimeter wave attenuation and brightness temperature due to atmospheric oxygen and water vapor", Radio Science 17(6), pp. 1455-1464, 1982.
11. J.R. Pierce and R. Kompfner, "Transoceanic Communication by Means of Satellites", Proc. IRE 47(3), pp. 372-380, 1959.
12. C.H. Papas, Theory of Electromagnetic Wave Propagation, McGraw-Hill Book Company, New York, Chapt. 6, 1965.
13. R.S. Lawrence, C.G. Little, and H.J.A. Chivers, "A Survey of Ionospheric Effects Upon Earth - Space Radio Propagation", Proc. IEEE, 52(1), pp. 4-27, 1964.
14. R.L. Thompson and J.A. Secan, "Geophysical Forecasting at AFGWC", in Solar-Terrestrial Prediction Proceedings Volume I: Prediction Group Reports, R.F. Donnelly, Ed., 1979 (for sale by the Superintendent of Documents, U.S. Government Printing Office, Washington, D.C. 20402, Stock No. 003-023-00041-9). p. 350-366.
15. S. Weisbrod and L.J. Anderson, "Simple Methods for Computing Tropospheric and Ionospheric Refractive Effects on Radio Waves", Proc. IRE, 47(10), pp. 1770-1777, 1959, Rome Air Development Center. AD 206 048
16. S. Weisbrod and L. Colin, "Refraction of VHF Signals at Ionospheric Heights", IRE Trans. Antennas Propagat., AP-8, pp. 107-109, 1960.
17. M.A. Kasha, The Ionosphere and Its Interaction with Satellites, Gordon and Breach, Science Publishers, New York, 1969.
18. E.C. Jordan and K.G. Balmain, Electromagnetic Waves and Radiating Systems, Prentice-Hall, Inc., Englewood Cliffs, NJ, 1963.
19. Y.L. Al'pert, Radio Wave Propagation and the Ionosphere Vol. 1-The Ionosphere, Consultants Bureau, New York, 1973.
20. B.H. Briggs and I.A. Parkin, "On the Variation of Radio Star and Satellite Scintillations with Zenith Angle", J. Atmosph. Terr. Phys., 25, pp. 339-366, 1963.
21. R.K. Crane, "Ionospheric Scintillation", Proc. IEEE, 65(2), pp. 180-199, 1977.

22. C.G. Little, G.C. Reid, E. Stiltner, and R.P. Merritt, "An Experimental Investigation of the Scintillation of Radio Stars Observed at Frequencies 223 and 456 Megacycles per Second from a Location Close to the Auroral Zone", J. Geophys. Res., 67(5), pp. 1763-1784, 1962.
23. J. Aarons, H.E. Whitney, and R.S. Allen, "Global Morphology of Ionospheric Scintillations", Proc. ISEE, 59(2), pp. 159-172, 1971.
24. J.M. Goodman, Ed., Effect of the Ionosphere on Space Systems and Communications, based on Ionosphere Effects Symposium held in Arlington, VA in Jan. 1975 and sponsored by the Naval Research Laboratory (for sale by the Superintendent of Documents, U.S. Government Printing Office, Washington, D.C. 20402, Stock Number 008-051-00064-0). (AD-A023 510)
25. J.M. Goodman, Editor-in-Chief, Effect of the Ionosphere on Radiowave Systems, based on the Ionospheric Effects Symposium held in Alexandria, Va., in April 1981 and jointly sponsored by the Office of Naval Research, the Naval Research Laboratory, and the Air Force Geophysics Laboratory (for sale by the Superintendent of Documents, U.S. Government Printing Office, Washington, D.C. 20402). (AD A-118 236)
26. J. Aarons, "High Latitude Morphology of Ionospheric Scintillations", Ref. 24, pp. 1-7.
27. K.C. Yeh, J.P. Mullen, J.R. Medeiros, R.F. daSilva, and R.T. Medeiros, "Ionospheric Scintillation Observations at Natal", Ref. 25, pp. 202-209.
28. J. Aarons, H.E. Whitney and E. MacKenzie, "Microwave Equatorial Scintillation Intensity During Solar Maximum", Ref. 25, pp. 193-197.
29. C.L. Rino, M.D. Cousins, and J.A. Klobuchar, "Amplitude and Phase Scintillation Measurements using the Global Positioning System", Ref. 25, pp. 253-261.
30. E.J. Fremouw, R.L. Leadabrand, R.C. Livingston, M.D. Cousins, C.L. Rino, B.C. Fair, and R.A. Long, "Early Results from the DNA Wideband Satellite Experiment -- Complex-Signal Scintillation", Radio Science, 13(1), pp. 167-187, 1978.
31. R.K. Crane, "Spectra of Amplitude and Phase Scintillation", Ref. 24, pp. 53-64.
32. H.E. Whitney and C. Cantor, "Amplitude and Fade Rate Statistics for Equatorial and Auroral Scintillations", Ref. 24, pp. 91-94.
33. K. Davies, "Ionospheric Predictions -- A Review of the State of the Art", Ref. 25, pp. 110-132.
34. J.R. Koster and R.W. Wright, "Scintillation, Spread F, and Transequatorial Scatter", J. Geophys. Res., 65(8), pp. 2303-2306, 1960.
35. J.M. Goodman and J. Aarons, "The Radiowave Propagation Environment -- Science and Technology Objectives for the 80's", Ref. 25, pp. xxi-xxx.

36. E.J. Fremouw, R.C. Livingston, and D.A. Miller, "On the Statistics of Scintillating Signals", J. Atmos. Terr. Phys., 42, pp. 717-731, 1980.

APPENDIX A. Refraction Error Above the Troposphere or Ionosphere  
in Terms of Error at the Upper Bounding Surface of  
the Medium

An expression will be derived here relating the refraction error seen by an elevated observer at an altitude above the top surface of the troposphere or ionosphere to the refraction error seen by an observer at the top surface of the troposphere or ionosphere. Referring to Fig. A-1, what is desired here is a relationship between  $\xi$  and  $\xi'$ , the refraction errors at altitudes  $h$  and  $h'$ , respectively, where  $h > h'$  and where  $h'$  is the altitude of the top surface of the troposphere or ionosphere. The propagation medium below altitude  $h'$  is assumed to possess refractive index gradients so that ray paths in this medium will in general be curved. Above altitude  $h'$  the refractive index is assumed to be constant so that ray paths are straight lines in this region.

It is assumed that the relationship between  $\xi'$  and  $\theta'$  is known a priori, along with the facts that  $\xi'$  is of first order smallness (on the order of a few milliradians for cases of interest here) and that first order changes in  $\theta'$  result in second order changes in  $\xi'$ .

Let  $D(h, \theta)$  represent the straight-line distance between an elevated observer at altitude  $h$  and a target on the surface of the earth, where  $\theta$  is the angle between the ground and the straight-line path to the observer, measured at the target. Referring again to Fig. A-1, one has

$$\overline{OT} = D(h, \theta), \quad (\text{A.1a})$$

$$\overline{O'T} = D(h', \theta'). \quad (\text{A.1b})$$

Now from the law of cosines for triangle  $CTO'$  one has

$$\overline{CO'}^2 = \overline{CT}^2 + \overline{O'T}^2 - 2\overline{CT}\overline{O'T} \cos(\theta' + \pi/2),$$

or

$$(r_0 + h')^2 = r_0^2 + D^2(h', \theta') + 2r_0 D(h', \theta') \sin \theta'. \quad (\text{A.2})$$

Solving for  $D(h', \theta')$ , one finds that

$$D(h', \theta') = (r_0^2 \sin^2 \theta' + 2r_0 h' + h'^2)^{1/2} - r_0 \sin \theta'. \quad (\text{A.3})$$

It will be useful to know how  $D(h', \theta')$  changes with small changes in  $\theta'$ . Taking the derivative of  $D(h', \theta')$  with respect to  $\theta'$ , one finds from Eq. (A.3) that

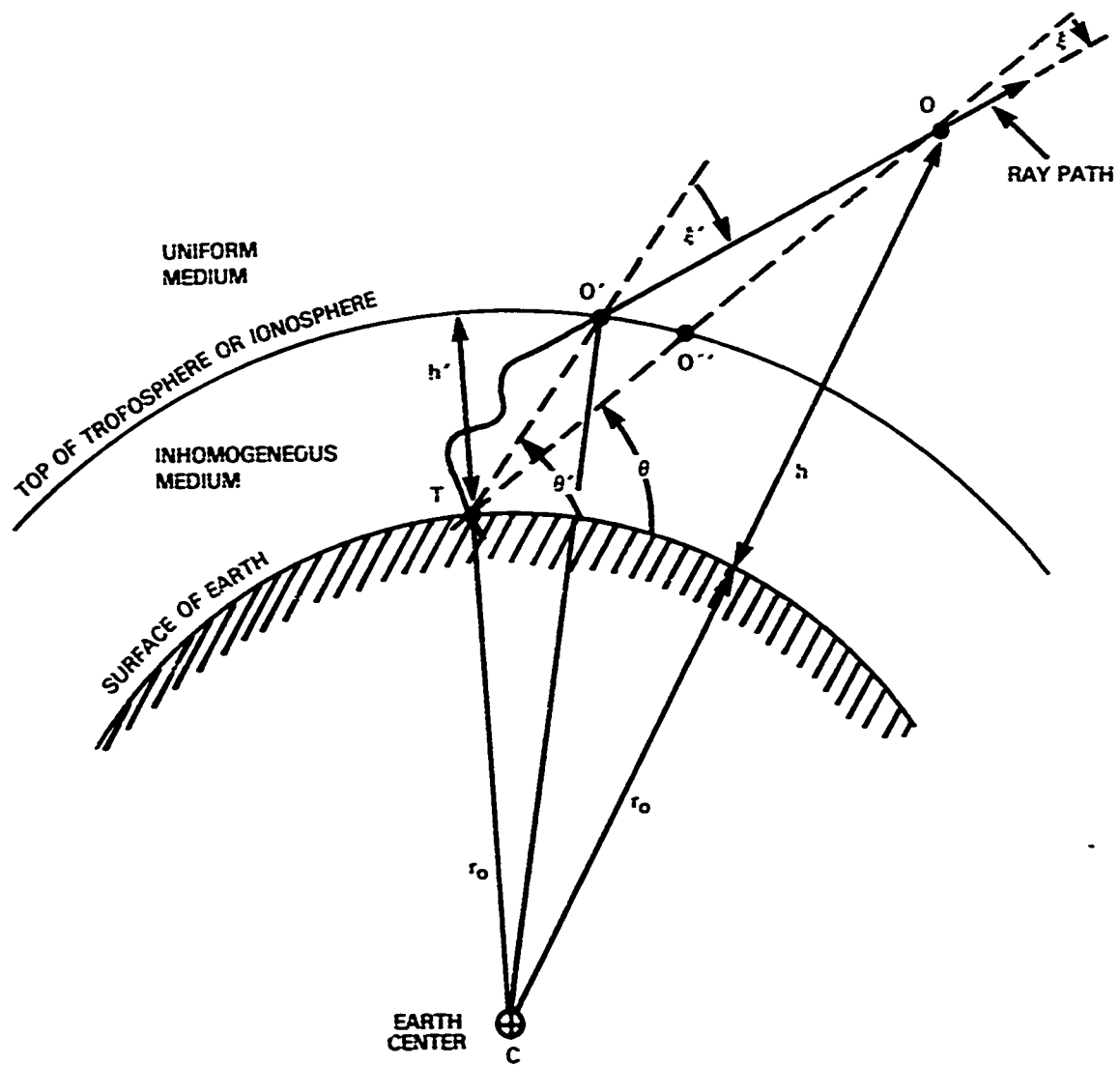


Fig. A-1 - Geometry of the refraction problem.

$$\frac{d}{d\theta'} D(h', \theta') = -D(h', \theta') \frac{\cos \theta'}{[\sin^2 \theta' + 2(h'/r_0) + (h'/r_0)^2]^{1/2}} \quad (\text{A.4})$$

One notes that

$$\frac{d}{d\theta'} D(h', \theta') \leq D(h', \theta') / [2h'/r_0]^{1/2},$$

or

$$\frac{|dD(h', \theta')|}{D(h', \theta')} \leq \frac{|d\theta'|}{[2h'/r_0]^{1/2}} \quad (\text{A.5})$$

By applying the law of cosines to triangle CTO (or more simply by replacing  $h'$  and  $\theta'$  with  $h$  and  $\theta$ , respectively, in Eq. (A.3)) one can next show that

$$D(h, \theta) = (r_0^2 \sin^2 \theta + 2r_0 h + h^2)^{1/2} - r_0 \sin \theta \quad (\text{A.6})$$

Angles  $\xi$  and  $\xi'$  can be related by an application of the law of sines to triangle TO'O. One finds that

$$\sin \xi = \frac{TO'}{TO} \sin \xi' = \frac{D(h', \theta')}{D(h, \theta)} \sin \xi' \quad (\text{A.7})$$

Since  $\xi'$  is very small one can replace  $\sin \xi'$  with  $\xi'$ . Furthermore, it is clear from triangle TO'O that

$$\xi = \xi' - (\theta' - \theta) \leq \xi' \quad (\text{A.8})$$

hence  $\xi$  is also very small and  $\sin \xi$  can be replaced with  $\xi$ . Eq. (A.7) can thus be written as

$$\xi \equiv \frac{D(h', \theta')}{D(h, \theta)} \xi'(\theta') \quad (\text{A.9})$$

where the dependence of  $\xi'$  on  $\theta'$  has been explicitly indicated.

It would be preferable if Eq. (A.9) could be written in terms of  $\theta$  alone, rather than in terms of both  $\theta$  and  $\theta'$ . Let  $\delta\xi$  represent the

change in the calculated value of  $\xi$  if  $\theta'$  is replaced with  $\theta$  in Eq. (A.9). One can then write

$$\delta\xi = \frac{\partial(h', \theta')}{\partial(h, \theta)} \delta\xi'(\theta') + \frac{\delta D(h', \theta')}{D(h, \theta)} \xi(\theta'),$$

or

$$\delta\xi = \left[ \frac{\delta\xi'(\theta')}{\xi'(\theta')} + \frac{\delta D(h', \theta')}{D(h', \theta')} \right] \frac{D(h', \theta')}{D(h, \theta)} \xi'(\theta'),$$

i.e.,

$$\delta\xi = \left[ \frac{\delta\xi'(\theta')}{\xi'(\theta')} + \frac{\delta D(h', \theta')}{D(h', \theta')} \right] \xi, \quad (\text{A.10})$$

provided that  $\theta' - \theta$  is of first order smallness. But from Eq. (A.8) it can be seen that

$$\theta' - \theta = \xi' - \xi < \xi'$$

hence the smallness of  $\theta' - \theta$  is established.

Now it was stated earlier that  $\xi'$  will exhibit a second order change if  $\theta'$  changes by first order. The quantity  $\delta\xi'/\xi'$  which appears in Eq. (A.10) will therefore be of first order smallness. Next, from inequality (A.5) it can be seen that the  $\delta D/D$  quantity which appears in inequality (A.10) will be on the order of  $(\theta' - \theta)/(2h'/r_0)^{1/2}$ . For the troposphere  $h' \approx 20$  miles and  $(r_0/2h')^{1/2} \approx 10$ ; for the ionosphere  $(r_0/2h')^{1/2}$  has a substantially smaller value. Since  $\theta' - \theta$  is on the order of a few milliradians, the quantity  $(\theta' - \theta)/(2h'/r_0)^{1/2}$  will be on the order of a few hundredths at most. Hence from Eq. (A.10) one sees that  $\delta\xi/\xi$  will be on the order of a few hundredths at most, i.e., the error incurred by replacing  $\theta'$  with  $\theta$  in Eq. (A.9) amounts to a few percent at most. One can thus write

$$\xi \approx \frac{\partial(h', \theta)}{\partial(h, \theta)} \xi'(\theta). \quad (\text{A.11})$$

More explicitly, by employing Eqs. (A.3) and (A.6) one obtains

$$\xi = \left[ \frac{(r_0^2 \sin^2 \theta + 2r_0 h' + h'^2)^{1/2} - r_0 \sin \theta}{(r_0^2 \sin^2 \theta + 2r_0 h + h^2)^{1/2} - r_0 \sin \theta} \right] \xi'(\theta). \quad (\text{A.12})$$

### APPENDIX B. Liquid Water Content of Rain-Laden Air

The absorption by water droplets of an electromagnetic wave propagating in air depends upon the total volume of water per unit volume of air rather than on the shapes and size distribution of the droplets, provided the droplet diameters are all much less than a wavelength. Now absorption in rain is generally given as a function of the hourly rain rate, while absorption in clouds or fog is given as a function of the mass (volume) of water per unit volume of air. In order to compare the values for rain and cloud/fog absorption it would be convenient to know the volume of water per unit volume of air for various rainfall rates. This relationship will be derived in the following.

To simplify matters let it be assumed that the raindrops have discrete diameters  $d_i$ ,  $i=1,2,\dots$ . Let  $R$  be the rain rate, let  $n(d_i;R)$  be the total number of raindrops per unit volume of air for rainfall rate  $R$ , and let  $v(d_i)$  be the velocity at which a raindrop of diameter  $d_i$  falls. Then one can write

$$R = \frac{\pi}{6} \sum_i [d_i^3 n(d_i;R) v(d_i)] \quad (B.1)$$

If  $W(R)$  is the volume of water per unit volume of air at rain rate  $R$  then one can also write

$$W(R) = \frac{\pi}{6} \sum_i [d_i^3 n(d_i;R)] \quad (B.2)$$

Let

$$n(d_i;R) = N_0(R) f(d_i;R) \quad (B.3)$$

where  $N_0(R)$  is the total number of rain drops per unit volume of air for rain fall rate  $R$  and where  $f(d_i;R)$  is the fraction of raindrops per unit volume having diameter  $d_i$  at rain rate  $R$ . Employing (B.3) in (B.1) and (B.2), one finds that

$$R = \frac{\pi}{6} N_0(R) \sum_i [d_i^3 f(d_i;R) v(d_i)] \quad (B.4)$$

$$W(R) = \frac{\pi}{6} N_0(R) \sum_i [d_i^3 f(d_i;R)] \quad (B.5)$$

Dividing Eq. (B.5) by Eq. (B.4) one readily obtains the result

$$W(R) = R \frac{\sum_i [d_i^3 f(d_i;R)]}{\sum_i [d_i^3 f(d_i;R) v(d_i)]} \quad (B.26)$$

This is the desired expression for the water content of rain-laden air in terms of the rain rate.

In order to obtain concrete numerical results from Eq. (B.6) it is necessary to have a distribution  $f(d_i; R)$  and the velocity function  $v(d_i)$ . A number of distribution functions are available; the one which will be employed here is the frequently used Laws and Parsons distribution as given by Medhurst\*, from which Table B-1 is obtained. The formula to be used for  $v(d_i)$  is obtained from Best\*\* for the standard I.C.A.N. (International Commission for Air Navigation) atmosphere, in particular

$$v(d) = \begin{cases} 9.32 \exp(0.0405z) \{1 - \exp[-(d/1.77)^{1.147}]\}, & 0.3 < d < 6.0 \\ 1.91 \exp(0.0290z) \{1 - \exp[-(d/0.316)^{1.754}]\}, & 0.05 < d < 0.3 \end{cases} \quad (B.7)$$

where  $v$  is in units of m/s, where  $d$  is in units of mm, and where  $z$  is the height above sea level in km.

The results of the calculations employing Eqs. (B.6), (B.7) and the Laws and Parsons distribution are given in Table B-2 and plotted in Fig. B-1.

---

\*R.G. Medhurst, "Rainfall attenuation of Centimeter Waves; Comparison of Theory and Measurement", IEEE Trans. Antennas and Propagation, AP-13, pp. 550-564, 1965

\*\*A.C. Best, "Empirical Formulae for the Terminal Velocity of Water Drops falling through the Atmosphere", Quart. J.R. Met. Soc., 76, pp. 302-311, 1950

TABLE B-1. Distribution of Raindrop Diameters for Various Rain Rates

(From R.G. Medhurst, Rainfall Attenuation of Centimeter Waves: Comparison of Theory and Measurement, IEEE Trans. Antennas and Propagat. AP-13, pp. 550-564 (1965), Copyright © 1965 IEEE, used by permission.)

Rain Rates (mm/hr) and Laws-Parsons Distribution (%)									
Drop Diam. (cm)	0.2	1.2	2.5	5.0	12.5	25.0	50.00	100.0	150.0
0.05	29.0	10.9	7.3	4.7	2.6	1.7	1.2	1.0	1.0
0.10	50.1	37.1	27.8	20.3	11.5	7.6	5.4	4.6	4.1
0.15	18.2	31.3	32.8	31.0	24.5	18.4	12.5	8.8	7.6
0.20	3.0	13.5	19.0	22.2	25.4	23.9	19.9	13.9	11.7
0.25	0.7	4.9	7.9	11.8	17.3	19.9	20.9	17.1	13.9
0.30		1.5	3.3	5.7	10.1	12.8	15.9	18.4	17.7
0.35		0.6	1.1	2.5	4.3	8.2	10.9	15.0	16.1
0.40		0.2	0.6	1.0	2.3	3.5	6.7	9.0	11.9
0.45			0.2	0.5	1.2	2.1	3.3	5.8	7.7
0.50				0.3	0.6	1.1	1.8	3.0	3.6
0.55					0.2	0.5	1.1	1.7	2.2
0.60						0.3	0.5	1.0	1.2
0.65							0.2	0.7	1.0
0.70									0.3

TABLE B-2 Liquid Water Content of Air for Various Rain Rates

Rain Rate (mm/hr)	Water Content (cm <sup>3</sup> /m <sup>3</sup> )
0.25	0.015
1.25	0.058
2.50	0.107
5.00	0.199
12.50	0.467
25.00	0.892
50.00	1.72
100.00	3.34
150.00	4.93

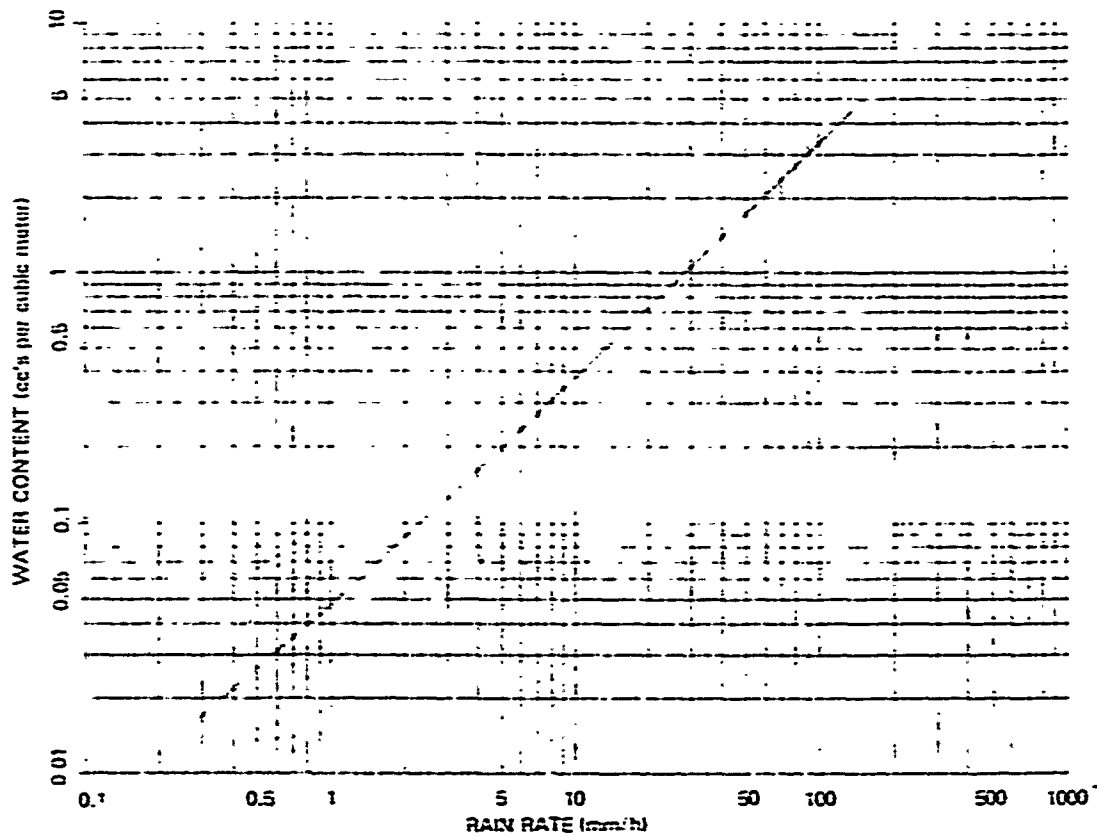


Fig. B-1 - Liquid water content of air vs. rain rate.

APPENDIX C. Ionospheric Refraction Error for an Elevated Observer  
in terms of Refraction Error at the Ground Target

The total bending  $\gamma$  of a ray is equal to the sum of the angles between the ray and the direct target-to-observer path at the ground and between the ray and the direct path at the observer (see Fig. C-1):

$$\gamma = \delta + \phi \quad . \quad (C.1)$$

One also has the following relationships between the other parameters in Fig. C.1\*:

$$\epsilon = \gamma - (\alpha - \beta), \quad (C.2)$$

$$\alpha - \beta = (N_0 - N) \times 10^{-6} \text{ctn} \alpha \equiv \Delta n \text{ctn} \alpha \quad , \quad (C.3)$$

$$a \cos \alpha_0 = (a+h) \cos \alpha \quad , \quad (C.4)$$

$$\alpha = \frac{\epsilon \tan \alpha}{\tan \alpha - \tan \alpha_0} \quad . \quad (C.5)$$

The quantity  $\Delta n$  is the difference between the ground refractive index,  $N_0 \times 10^{-6}$ , and the refractive index at the observer,  $N \times 10^{-6}$ .

One now employs Eq. (C.3) in Eq. (C.2) in order to obtain

$$\gamma = \epsilon + \Delta n \text{ctn} \alpha \quad . \quad (C.6)$$

Next, with the aid of Eq. (C.4) one can show that

$$\text{ctn} \alpha = \frac{a \cos \alpha_0}{[(a+h)^2 - a^2 \cos^2 \alpha_0]^{1/2}} \quad (C.7)$$

---

\*R. Weisbrod and L.J. Anderson, "Simple Methods for Computing Tropospheric and Ionospheric Refraction Effects on Radio Waves", Proc. IRE, 47(10), pp. 1770-1777, 1959

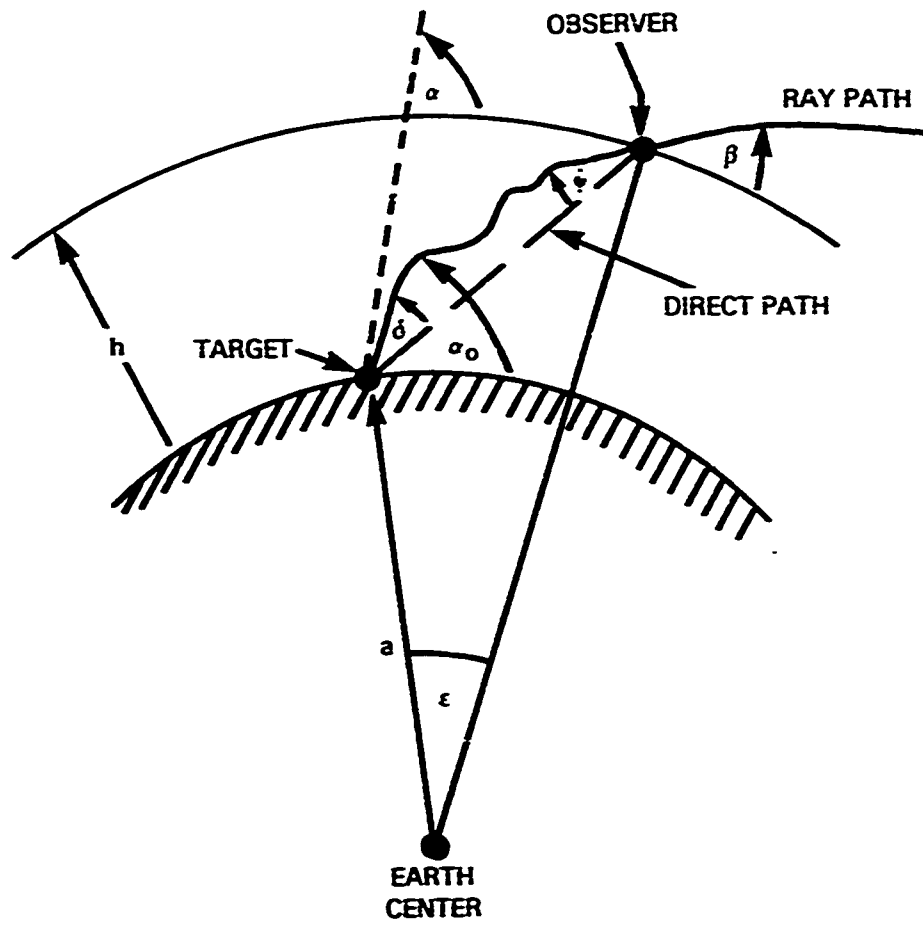


Fig. C-1 - Geometry of the refraction error computation.

Employing this in Eq. (C.6), one finds that

$$\gamma = \epsilon + \frac{a\Delta n \cos \alpha_0}{[(a+h)^2 - a^2 \cos^2 \alpha_0]^{1/2}} \quad (C.8)$$

If this is in turn employed in Eq. (C.1), one can obtain the result

$$\theta = \epsilon + \frac{a\Delta n \cos \alpha_0}{[(a+h)^2 - a^2 \cos^2 \alpha_0]^{1/2}} - \delta \quad (C.9)$$

Eq. (C.5) can be solved for  $\epsilon$  with the result

$$\epsilon = \delta \left[ 1 - \frac{\text{ctn} \alpha}{\text{ctn} \alpha_0} \right] \quad (C.10)$$

One then employs (C.7) in this equation in order to obtain

$$\epsilon = \delta \left[ 1 - \frac{a \sin \alpha_0}{[(a+h)^2 - a^2 \cos^2 \alpha_0]^{1/2}} \right] \quad (C.11)$$

When this expression for  $\epsilon$  is substituted into Eq. (C.9) one finds that

$$\phi = \frac{\Delta n \cos \alpha_0 - \delta \sin \alpha_0}{[(1+h/a)^2 - \cos^2 \alpha_0]^{1/2}} \quad (C.12)$$

This is the desired result for the refraction error at the observer,  $\theta$ , in terms of the refraction error at the target,  $\alpha_0$ .

The notation for the geometric parameters used in the main body of of this report differ from those employed here. In particular,  $\phi$  was represented by  $\Delta \tilde{\alpha}_0$ ,  $\delta$  by  $\Delta \tilde{\alpha}_G$ ,  $\alpha_0$  by  $\theta$ , and  $a$  by  $r_0$ . In terms of these parameters Eq (C.12) assumes the form

$$\Delta \tilde{\alpha}_0 = \frac{\Delta n \cos \theta - \Delta \tilde{\alpha}_G \sin \theta}{[(1+h/r_0)^2 - \cos^2 \theta]^{1/2}} \quad (C.13)$$